Coseismic deformation of the ground during large-slip strike-slip ruptures: Finite evolution of "mole tracks"

T.A. Little[1], P. Morris[1], M.P. Hill[2], J. Kearse[1], R.J. Van Dissen[2], J. Manousakis[3], D. Zekkos[4], and A. Howell[2]

[1]School of Geography, Environment & Earth Sciences, Victoria University of Wellington, Wellington 6040, New Zealand
[2]GNS Science, Lower Hutt 5040, New Zealand
[3]Elxis Group, Athens 115 28, Greece
[4]Department of Civil and Environmental Engineering, University of California at Berkeley, Berkeley, California 94720-1710, USA

ABSTRACT

To evaluate ground deformation resulting from large (~10 m) coseismic strike-slip displacements, we focus on deformation of the Kekerengu fault during the November 2016 M_w 7.8 Kaikōura earthquake in New Zealand. Combining post-earthquake field observations with analysis of high-resolution aerial photography and topographic models, we describe the structural geology and geomorphology of the rupture zone. During the earthquake, fissured pressure bulges ("mole tracks") initiated at stepovers between synthetic Riedel (R) faults. As slip accumulated, near-surface "rafts" of cohesive clay-rich sediment, bounded by R faults and capped by grassy turf, rotated about a vertical axis and were internally shortened, thus amplifying the bulges. The bulges are flanked by low-angle contractional faults that emplace the shortened mass of detached sediment outward over less-deformed ground. As slip accrued, turf rafts fragmented into blocks bounded by short secondary fractures striking at a high angle to the main fault trace that we interpret to have originated as antithetic Riedel (R′) faults. Eventually these blocks were dispersed into strongly sheared earth and variably rotated. Along the fault, clockwise rotation of these turf rafts within the rupture zone averaged ~20°–30°, accommodating a finite shear strain of 1.0–1.5 and a distributed strike slip of ~3–4 m. On strike-slip parts of the fault, internal shortening of the rafts averaged 1–2 m parallel to the R faults and ~1 m perpendicular to the main fault trace. Driven by distortional rotation, this contraction of the rafts exceeds the magnitude of fault heave. Turf rafts on slightly transtensional segments of the fault were also bulged and shortened—relationships that can be explained by a kinematic model involving "deformable slats." In a paleoseismic trench cut perpendicular the fault, one would observe fissures, low-angle thrusts, and steeply dipping strike-slip faults—some cross-cutting one another—yet all may have formed during a single earthquake featuring a large strike-slip displacement.

■ INTRODUCTION

The term "mole track" describes deformed and upheaved ground along strike-slip ruptures. The analogy was introduced by Koto (1893) in his monograph

Timothy Little [iD] https://orcid.org/0000-0002-5783-6429

about the October 1891 M_s 8.0 Mino-Owari earthquake near Tokyo. In this (p. 328), he described a strike-slip rupture on the Nobi alluvial plain as follows:

> "It strikes across hills and paddy fields alike, cutting up the soft earth into enormous clods and raising them above the surface. *It resembles the pathway of a gigantic mole…* [his italics]"

Although its meaning seems imprecise and varies between workers, the term "mole track" has been in common use since at least the 1970s. We use it here to refer to uplifted mounds of broken and fractured ground that form in a repeating pattern along strike-slip earthquake ruptures. While it is well known that mole tracks initiate from localized compression of the ground in contractional stepovers between overlapping strike-slip fractures (e.g., Bergerat et al., 2003; Lin et al., 2004), little or no work has been done to evaluate: (1) how mole tracks and their bounding structures may evolve as a function of increasing fault displacement; or (2) what morphology or structures characterize rupture zones that have accrued an especially large (e.g., 6–10 m) strike slip. Understanding processes by which the ground progressively deforms to accommodate large coseismic displacements would facilitate accurate mapping and documentation of coseismic slip in the landscape and identification of ancient earthquakes in paleoseismic trenches.

In this paper, we focus on the rupture of the 14 November 2016 M_w 7.8 Kaikōura earthquake in New Zealand. This earthquake ruptured a diverse assemblage of faults in the northeastern part of the South Island along an ~180 km length of the transpressional Pacific-Australia plate boundary (Litchfield et al., 2018). Of these, the Kekerengu fault, a chiefly dextral strike-slip structure, experienced the largest coseismic surface displacement (as much as ~12 m; Kearse et al., 2018). Rupture on this fault propagated northeastward (e.g., Cesca et al., 2017; Holden et al., 2017) across a near-coastal landscape of rolling hills, alluvial terraces, and agricultural fields, much of it grass covered. Dextral slip on this part of the fault varied along strike between 6 and 12 m and was accompanied by a small heave (typically <1 m) between slight transpression and slight transtension (Kearse et al., 2018). Geodetic data and geological field surveys processed after the earthquake provide precise measures of the coseismic displacement vector at many points along this trace (e.g., Hamling et al., 2017; Kearse et al., 2018; Zinke et al., 2019; Howell et al., 2020). The area is thus a "natural laboratory" of coseismic ground deformation—one where

structures observed along the rupture can be attributed to known amounts and directions of displacement.

Soon after the earthquake, high-resolution photography and topographical mapping of the rupture zone was done in selected areas using remotely piloted aircraft systems (RPAS, or "drones"). In addition, lidar surveys and accompanying scans of optical imagery were flown across most of the fault ruptures by aircraft, yielding digital terrain models (DTMs) at resolutions as small as 20 cm. In conjunction with direct field observations on the ground, these high-resolution data sets, especially the RPAS imagery, captured the structural morphology of the rupture in detail prior to its later rapid erosion and degradation. In this paper, our chief goals are (1) to identify features diagnostic of very large strike-slip earthquakes, (2) to reconstruct the progressive development of the strike-slip rupture zone in response to an unusually large magnitude of slip to derive a conceptual kinematic model for coseismic strike-slip ground deformation, including the development of mole tracks, and (3) to assess the relative contributions of distributed versus discrete slip. Finally, we will evaluate how differing local kinematics (e.g., strike slip, transpression, transtension) and ground mechanical properties (e.g., granular versus cohesive soils) may influence the morphology of natural mole tracks.

■ STRUCTURAL NOMENCLATURE

Analogue modeling experiments have provided a conventional framework for labeling brittle fractures in strike-slip fault zones. A common experimental setup places a cover layer of clay or sand above a vertical strike-slip fault in the basement (e.g., Cloos, 1928; Riedel, 1929). For this idealized "Riedel" boundary condition, initial deformation on the surface of the cover pack typically includes an en echelon array of synthetic strike-slip faults (synthetic Riedel [R] faults) that typically strike at ~15°–20° to the underlying basement fault (Fig. 1A), an angle that is thought to be governed by the angle of internal friction of the material (φ) through Coulomb fault mechanics (e.g., Tchalenko and Ambraseys, 1970; Dooley and Schreurs, 2012), although the structure in the subsurface is three-dimensional (3-D) and more complex than that on the surface (e.g., Naylor et al., 1986). Whereas R faults in experiments are nearly always present as early-formed structures—regardless of the material properties and specific boundary conditions—their conjugates (called antithetic Riedel faults, R′) are not always developed (Dooley and Schreurs, 2012). In cases where they are expressed, R′ faults typically strike at 65°–70° relative to the basement fault, as is consistent with Coulomb faulting theory (e.g., Wilcox et al., 1973). Due to the effect of cohesion, clay packs, unlike sand, may fail not only in shear but also by extension fracturing. In theory, extension fractures (tensile [T] cracks) are predicted to form parallel to σ_1 and orthogonal to σ_3. In an elastically isotropic material deforming by transcurrent simple shearing, σ_1 is predicted to trend at ~45° to the strike of the zone (e.g., Teyssier et al., 1995). Finally, experiments and field studies indicate that stress trajectories are perturbed near the tips of the early-formed R faults (Naylor et al., 1986; see Fig. 1B). In the extensional

quadrant of the R fault, this can result in nucleation of new splay faults (R_{splays}) or fault-tip propagation at a relatively high strike angle relative to the main fault, whereas in the contractional quadrant, R-fault tips may propagate at a low strike angle (R_{low}). Stress rotation is expected to be strongest inside the contractional stepovers between overlapping R faults. Here, up-bulging of the deformed cover (e.g., clay or sand) is typical, and the flanking R faults, dipping inward, typically accrue some reverse dip slip (e.g., Schreurs, 1994, 2003). If the stress rotation in plan view is large enough (Fig. 1B), synthetic cross-faults (P faults) may form (Naylor et al., 1986). These strike in the opposite quadrant relative to the basement fault and are subvertical (Fig. 1A). A mixture of R_{low} and/or P faults may link earlier-formed R faults. Such linkage eventually results in a longer, coalesced fault with further slip typically being localized into this master fault, especially in dry sand (which tends to strain-soften; e.g., Dooley and Schreurs, 2012). The throughgoing fault is referred to as a Y fault if it strikes subparallel to the basement fault.

Whereas this nomenclature provides a scheme for classifying fractures in strike-slip deformation zones based on their attitude and slip sense, there are difficulties in applying it to natural earthquake rupture zones. These include the simplicity of the experimentally imposed boundary conditions relative to natural earthquake ruptures, which propagate coseismically and are influenced by dynamic stresses. In addition, the published experiments are mostly limited to finite shear strains of <0.5 in modeled cover layers that are much thicker than the total strike-slip magnitude. While experiments can provide insight into fault nucleation, they are less successful in documenting the progressive structural evolution of deformed ground adjacent to a natural strike-slip fault rupture subject to a large coseismic displacement, especially where those ground materials have been detached into a thin, cohesive layer that is highly deformed. In addition, (1) the properties of the natural ground materials are likely to differ from dry sieved sand, moist clay, or commonly used viscous analogues; (2) real faults generally break along preexisting faults that typically extend to within a few meters from the free surface at the time of an earthquake; and (3) surface topography probably contributes to local complexities of the stress field and hence to surface rupture morphology. The experimental studies indicate that small changes in the boundary conditions of the rig (e.g., distributed shear at depth rather than slip on a discrete basement fault) or in the rheological properties of the deformed material can strongly influence structures that are developed in a fault zone (Dooley and Schreurs, 2012).

In this paper, we examine a natural fault rupture zone that was subject to a large strike-slip earthquake displacement. We define "rupture zone" as the swath of ground within which fractures (>10 cm long) are observed breaking the ground surface. Along the Kekerengu fault, the width of this zone of disturbed ground (W_{RT} in Fig. 1C) was typically 5–10 m. Surveys of once-linear fence lines deformed during the 2016 earthquake reveal that >80% of the strike slip was accommodated within this approximate width (Kearse et al., 2018), and that a smaller, diffuse component of off-fault deformation was accommodated beyond the rupture zone (Fig. 1C). As measured from deflection of fence lines during the 2016 Kaikōura earthquake rupture of the Kekerengu fault and 2010

Figure 1. (A) Conventional classification of fractures in strike-slip rupture zones, based on their inception attitude and slip sense, assuming Coulomb fault mechanics (e.g., Tchalenko and Ambraseys, 1970; Naylor et al., 1986). R—synthetic Riedel fault; R′—antithetic Riedel fault; T—tensile fracture; P—synthetic linking fault; Y—fault striking parallel to the main fault. Angle φ is the angle of internal friction. (B) Schematic trajectories of σ_1 showing predicted deflection near tips of R faults and predicted traces of local secondary faults or splays, assuming Coulomb fault mechanics (after Naylor et al., 1986). (C) Cartoon defining fault rupture terminology used in this paper (width of zones is not to scale). The total displacement vector (relative motion of the upper block relative to the lower) makes an angle, α, relative to the strike of the main fault, with positive angles defined to be transpressive. "Rupture zone" refers to the region in which discrete faults and fissures break the ground surface, whereas the total deformation zone, which is wider, also includes two outer zones of off-fault distributed shear deformation without ground rupturing. The inner high-strain zone contains the most strongly disturbed ground. It contains "turf rafts" (decoupled from underlying material) that have rotated about a vertical axis. Initially, these are bounded by synthetic Riedel faults (R); later they are variably bounded by low-angle thrust faults on at least one side and gaping fissures on others. After rotation, turf rafts may remain in part attached to one of the main fault blocks but unattached from the other along a low-angle (oblique-slip) thrust fault. "F" refers to fractures or fissures, the displacement of which is dominated by extensional gaping. Short secondary fractures labeled "2" strike at a high angle to the main fault trace, accumulate antithetic slip, and cross-cut (and disaggregate) the previously formed turf rafts. Y faults refer to strike-slip fault strands striking parallel to the main fault trace as expressed regionally and probably at depth. The angles β_o and β_i refer to the outer (less deformed, R) and inner (rotated, R_{rot}) strikes of synthetic Riedel faults. "S" refers to the mean spacing of the Riedel faults as measured parallel to the overall trace of the main fault in the outer rupture zone. W_{RT}—total rupture width, W_{DT}—total deformation width, W_{RI}—inner rupture zone width, R_{low}—low-angle Riedel faults, R_{splay}—Riedel fault-tip splay faults.

Darfield earthquake rupture of the Greendale fault (this ruptured the ground ~250 km to the SW of the study area), total deformation widths (W_{DT} in Fig. 1C) are commonly 20–90 m, and in places 100–300 m (Quigley et al., 2012; Litchfield et al., 2014; Kearse et al., 2018). Optical image correlation (OIC) analysis of satellite imagery (Zinke et al., 2019), and differencing of 3-D point clouds derived from aerial photographs (Howell et al., 2020) along the Kekerengu fault after the 2016 earthquake yields estimates of total displacement over an aperture of several hundred meters that are as much as ~10% greater than field surveys of displacement collected over an aperture of 10–20 m.

Only some of the aforementioned fracture classifications were useful (or identifiable) to us in our field work. These include R faults (and their two variants, R_{splays} and R_{low} faults) and Y faults. We also observed open or gaping extension fractures, in some cases as wing cracks extending from fault tips. For this study, we descriptively refer to gaping fractures as fissures (F) rather than as tensile fractures (T) because many of the fractures accumulated some shear displacement and may not have nucleated as true tensile fractures, which is a genetic interpretation. In our nomenclature, a "turf raft" is a coseismically deformed strip of grass-colonized turf or soil together with an underlying layer of detached clay-rich sediment. The rafts we observed were mostly bounded by R faults, but in some cases by gaping fissures (F). Little-deformed parts of the rupture zone where the turf rafts and their bounding structures seem approximately in situ and unrotated we refer to as the "outer rupture zone." In the inner part of the rupture zone, by way of contrast, the turf rafts have been torn away from bounding R faults, rotated about vertical axes, and up-bulged and/or thrust over adjacent less-deformed turf. This highly deformed, inner part of the rupture zone, which we call the "inner high-strain zone," has a width W_{RI} (Fig. 1C). Inside it, the clockwise-rotated equivalents of the original of Riedel faults are called R_{rot} faults, whereas other, much more numerous fractures strike at a high angle to the main fault trace. Descriptively, we call the latter "secondary fractures" ("2" in Fig. 1C). The "2" fractures cross-cut the R_{rot} faults, and their superposition broke up the originally elongate turf rafts into fragments of more nearly equant shape.

■ PREVIOUS WORK ON MOLE TRACKS

Surprisingly little work has focused on the origin, and especially evolution, of mole tracks. Deng et al. (1986) described surface features along the 1920 M_s 8.7 Haiyuan earthquake in the northeastern Tibetan Plateau and the 1973 M_s 7.9 Luhuo earthquake in the central-eastern Tibetan Plateau. Armijo et al. (1989) described ground deformation on seismogenic strike-slip faults in eastern Tibet. Bergerat et al. (2003) described fracture patterns and pressure ridges (mole tracks) developed on Holocene lava flows of the South Iceland seismic zone. These (and other) studies document a predominance of R faulting and the mechanical role of coherent surface sediments, including frozen ground, in the forming of "rectangular turf shells" or "turf carpets," bounded by "fissures" that have rotated and thrust along their margins in response to distributed

strike-slip shear beneath them. Between adjacent fissures, strips of shortened turf are described as being up-bulged into pressure ridges. These are typically arranged in an en echelon pattern. Ground deformation resulting from several recent strike-slip earthquakes of M_w 6.9–7.8 in northern Tibet, including the 2001 Kunlun earthquake and the 2010 Yushu earthquake, has been described from field work (Rao et al., 2011; Lin et al., 2004, 2011; Jin and Wang, 2009; Lin and Nishikawa, 2011). During the Kunlun earthquake, mole tracks, as high as ~3 m formed when as much as 7 m of strike slip was accumulated along individual fault strands in cohesive alluvial soils, typically within an inner high-strain zone that was 5–10 m wide (Lin et al., 2004). The bulges coincided with rounded to angular folds of a deformed surficial layer, largely frozen, that was as thick as 2.5 m and that was decoupled from its substratum. The mole track–bounding fractures were variably identified as R faults or fissures. Ground deformation associated with the 2010 Greendale strike-slip earthquake in New Zealand (M_w 7.1, maximum slip ~5.4 m) was described by Quigley et al. (2012), with slip distributions across the fault being documented in detail by Litchfield et al. (2014). As measured by deflected fence lines, the alluvial sediments affected by this earthquake were deformed across a total deformation zone that was as much as 300 m wide (average 80–90 m), most of it not marked by macroscopic fracturing. Unlike in most of the aforementioned case studies, antithetic Riedel faults (R′) were common in the rupture zone of the Greendale fault, which broke through a previously little-deformed alluvial sequence inferred to be tens to hundreds of meters thick. Most recently, Kearse et al. (2018) described ground deformation along the Kekerengu fault during the M_w 7.8 2016 Kaikōura earthquake, including progressive rotation of detached turf strips separated from one another by R faults that later opened as extensional fissures.

■ METHODS

Our study focuses on the easternmost ~8 km of the 2016 on-land rupture of the Kekerengu fault (Figs. 2A, 2B). To the east of the Kekerengu River (Fig. 2B), the rupture trace was examined and photographed on foot within a week of the earthquake, while to the west, it was studied within six weeks of the earthquake. Exposures of the fault plane were common along this trace—a result of steep canyon walls being laterally displaced by ~10 m, thus exhuming free faces in bedrock (Kearse et al., 2018, 2019). The faces mostly dipped steeply to the northwest (green arrows, Fig. 2B). At one location (Fig. 2B, white square in area C), fault displacements were measured by repeat surveying of fenceposts and the walls of a preexisting (now offset) paleoseismic trench before and after the earthquake (Kearse et al., 2018; Morris, 2020). Elsewhere, displacement vectors were obtained by surveying the offset of fences, roads, landforms, and other linear features (Kearse et al., 2018) and by differencing of photogrammetry-based 3-D point clouds derived from aerial photographs taken before and after the earthquake (Howell et al., 2020). Of these three methods, only the first and last ones are able to capture the heave, thus allowing reliable azimuths and total magnitudes of coseismic displacement to be obtained (Fig. 2B, red arrows). The
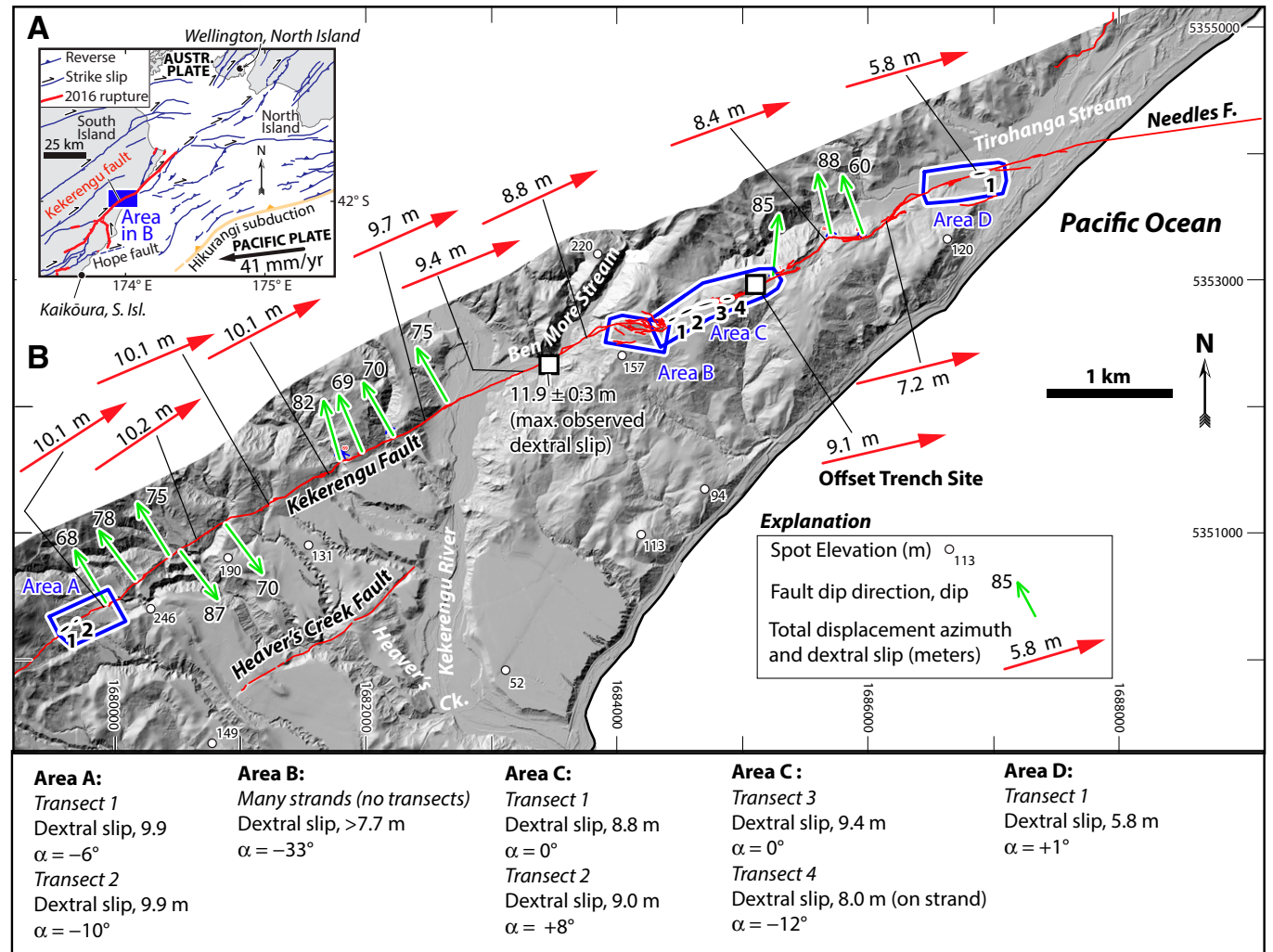
Figure 2. (A) Tectonic setting of the Kekerengu fault (New Zealand) on the Australia-Pacific plate boundary, showing selected earthquake ruptures associated with the M$_w$ 7.8 Kaikōura earthquake in red (from Litchfield et al., 2018), and study area along the Kekerengu fault as a blue box. The topography of the field area is depicted with a grey hillshade model. The white area to the right is the Pacific Ocean whereas that to the left is the onshore region to the west of the study area. Plate motion vector—Pacific plate relative to Australian—is from Beavan et al. (2002). (B) Lidar-based shaded-relief digital elevation model of eastern Kekerengu fault. 2016 Kaikōura earthquake rupture traces are shown in red. Blue polygons show the location of areas in which detailed unmanned aerial vehicle–based photographic and topographic data were analyzed (Supplemental Material Item S3 [text footnote 1]). Within these areas, the location of fault-parallel transects for this study are identified and numbered (Supplemental Material Item S2). Red arrows show relative displacement azimuths across the fault (north block relative to south) and total dextral-slip magnitude as measured using three-dimensional point cloud differencing by Howell et al. (2020). Two spot dextral-slip measurements derived from field surveys of offset features (black boxes: at maximum observed dextral-slip and at offset trench) are from Kearse et al. (2018). Text in the bottom panel specifies kinematic boundary conditions for each area or transect, where the angle α is the angle between the local displacement vector and fault strike (positive where transpressional; see Fig. 1C). Grid marks and coordinates (in meters of easting and northing) refer to the New Zealand Transverse Mercator 2000 (NZTM2000) projection as based on the NZGD2000 datum and the GRS80 reference ellipsoid.

published displacement studies documented a total slip (mostly horizontal and dextral) that ranged, from northeast to southwest, from ~6 m near the coast to a maximum of ~12 m near Ben More Stream (Fig. 2B, white square southwest of area B) to 10–11 m to the west of Kekerengu River.

In addition to our on-ground field observations, we analyzed orthophotographs created from optical images collected by using remotely piloted aircraft systems (RPAS, or "drones") along the fault rupture zone. Images were collected in seven different swaths between one and two weeks after the earthquake as part of the Geotechnical Extreme Event Reconnaissance (GEER) initiative in collaboration with workers from GNS Science (Lower Hutt, New Zealand) and the University of Michigan (Ann Arbor, Michigan, USA)–University of California at Berkeley (Berkeley, California, USA) (Zekkos et al., 2018). These aerially surveyed swaths, several of them contiguous to one another, encompass areas A, B, C, and D in Figure 2B. More than 3000 aerial photographs were taken at mean heights of 30–60 m above the ground and yielded an average resolution of 2–3 cm per pixel (Item S1 in the Supplemental Material[1]). In each swath area, the optical images were used to create a digital surface model (DSM) and 3-D point cloud, using the structure-from-motion (Carrivick et al., 2016) technique and a set of ground control points collected with an RTK (real-time kinematic) GPS system (Zekkos et al., 2018; Hill, 2020). The DSMs are in excellent agreement (mean difference of 0.2 m, standard deviation of 0.23 m) with 1 m aerial lidar-based models of the same region, but more finely resolved (Zekkos et al.,

2018). Because the RPAS-derived orthophotography was flown within days after the earthquake, and at a much lower altitude than the photography collected from aircraft during the lidar surveys (two to six weeks after the earthquake), the imagery has a higher resolution and the imaged ground surface had experienced almost no erosion. We found the RPAS-derived orthophotography to be especially valuable for structural analysis of ground deformation because individual cracks and faults are clearly imaged at the 10 cm scale, and their effect on—or offset of—other optically resolvable features, such as fences, stock tracks, and clumps of grass, could be observed. In each study area, structures were mapped onto an interpreted layer in a GIS program (MapInfo Professional), and their traces classified using the scheme in Figure 1C. In addition, the strikes of fractures, rupture zone inner and total widths (W_{RI} and W_{RT}), and mean spacing of R faults (S) were digitized, averaged, and tabulated (Table 1). Finally, selected parts of the DSM were queried to measure the local structural relief and area of deformational bulges in the rupture zone.
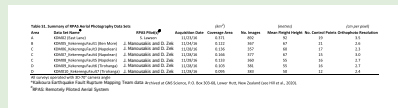
■ MORPHOLOGY AND STRUCTURAL GEOLOGY OF THE 2016 KEKERENGU FAULT RUPTURE ZONE

The surface expression of the fault rupture varied with ground type and local fault kinematics. We use the past tense in our descriptions below

TABLE 1. SUMMARY OF TRANSECT MEASUREMENTS, KEKERENGU FAULT, NEW ZEALAND

Transect site	Fault strike (°)	Fault throw* (m)	Displacement azimuth† (°)	Displacement magnitude† (m)	Displacement angle (α)† (°)	Displacement heave (m)	Riedel faults, mean spacing (S)§ (m)	Rupture zone, mean total width (W_{RT}) (m)	Rupture zone, mean inner width (W_{RI}) (m)	Outer zone Riedel faults (R) mean strike angle ($β_o$) (°)	Inner zone rotated Riedel faults (R_{rot}) mean strike angle ($β_i$) (°)
		+ve, NW up			+ve, contractional						
Area A, transect 1	062	0.6	56	10.1	−6	−1.1	1.6	9.8 ± 5.4 (n = 15)	5.5 ± 1.9 (n = 28)	28 ± 4 (n = 73)	48 ± 14 (n = 148)
Area A, transect 2	066	0.6	56	10.1	−10	−1.8	1.2	4.6 ± 1.2 (n = 14)	3.0 ± 1.0 (n = 18)	24 ± 3 (n = 21)	65 ± 21 (n = 85)
Area C, transect 1	065	0.1	65	8.9	0	0.0	2.6	6.8 ± 2.5 (n = 13)	1.9 ± 0.9 (n = 15)	24 ± 5 (n = 36)	51 ± 19 (n = 36)
Area C, transect 2	057	1.0	65	9.0	8	1.3	2.4	3.8 ± 1.5 (n = 30)	2.0 ± 0.7 (n = 30)	26 ± 9 (n = 60)	53 ± 18 (n = 75)
Area C, transect 3	066	0.1	66	9.4	0	0.0	2.5	5.2 ± 3.2 (n = 33)	1.6 ± 0.5 (n = 31)	27 ± 6 (n = 73)	55 ± 15 (n = 95)
Area C, transect 4	082	−0.6	70	8.0	−12	−1.7	2.0	6.9 ± 0.7 (n = 9)	3.0 ± 1.3 (n = 14)	20 ± 4 (n = 29)	39 ± 12 (n = 105)
Area D, transect 1#	074	−1.0	75	3.5	1	0.1	0.1	3.1 ± 1.1 (n = 16)	1.5 ± 0.6 (n = 16)	43 ± 5 (n = 29)	92 ± 30 (n = 39)
Mean of sites				9.3			2.1	6.2	2.8	25	52
Standard deviation				0.8			0.6	2.2	1.4	3	9

(*continued*)

Little et al. | Evolution of mole tracks

TABLE 1. SUMMARY OF TRANSECT MEASUREMENTS, KEKERENGU FAULT, NEW ZEALAND (*continued*)

Transect site	Mean rotation $(\beta_i-\beta_o)$ (°)	Outer zone fissures (F) mean strike angle (β_o) (°)	Inner zone secondary fractures ("2") mean strike angle (β_i) (°)	Maximum bulge relief (m)	Measured excess area of bulges** (m^2)	Assumed detachment depth (m)	Area-balancing calculated shortening (Δs)** (m)	Original raft length (L_o)** (m)	Area-balancing calculated longitudinal strain (ε)** $(\varepsilon = \Delta s / L_o)$
							+ve, contractional		+ve, contractional
Area A, transect 1	20	52 ± 11 (*n* = 152)	84 ± 20 (*n* = 573)	0.61 ± 0.16 (*n* = 6)	2.19 ± 0.84 (*n* = 6)	1.1 ± 0.4	1.99 ± 1.05	9.37 ± 1.9	0.21 ± 0.12
Area A, transect 2	41	48 ± 6 (*n* = 14)	91 ± 23 (*n* = 56)	0.37 ± 0.10 (*n* = 3)	3.10 ± 0.90 (*n* = 3)	1.1 ± 0.4	2.82 ± 1.31	3.20 ± 0.3	0.88 ± 0.42
Area C, transect 1	27	52 ± 12 (*n* = 55)	86 ± 23 (*n* = 109)	0.53 ± 0.15 (*n* = 6)	1.18 ± 0.27 (*n* = 5)	1.1 ± 0.4	1.07 ± 0.46	4.67 ± 1.52	0.23 ± 0.12
Area C, transect 2	27	64 ± 13 (*n* = 33)	96 ± 21 (*n* = 611)	0.50 ± 0.17 (*n* = 6)	1.64 ± 0.96 (*n* = 6)	1.1 ± 0.4	1.49 ± 1.03	7.53 ± 1.56	0.20 ± 0.14
Area C, transect 3	28	56 ± 8 (*n* = 55)	98 ± 19 (*n* = 295)	0.35 ± 0.05 (*n* = 4)	0.70 ± 0.43 (*n* = 4)	1.1 ± 0.4	0.63 ± 0.45	3.52 ± 0.62	0.18 ± 0.13
Area C, transect 4	10	48 ± 10 (*n* = 25)	83 ± 20 (*n* = 136)	0.45 ± 0.18 (*n* = 6)	1.71 ± 0.73 (*n* = 6)	1.1 ± 0.4	1.55 ± 0.87	3.80 ± 1.08	0.18 ± 0.26
Area D, transect 1#	49	N/A	N/A	0.13 ± 0.05 (*n* = 6)	0.23 ± 0.13 (*n* = 6)	0.3 ± 0.2	0.77 ± 0.69	2.35 ± 0.59	0.33 ± 0.31
Mean of sites	**26**	**53**	**90**	**0.47**	**1.75**		**1.59**		**−0.32**
Standard deviation	**10**	**6**	**6**	**0.10**	**0.83**		**0.76**		**0.25**

Note: See Figure 1C for definitions of α, *S*, β_o, β_i, W_T, W_{inner}, R faults, R_{rot} faults, fissures (F), and secondary fractures ("2"); see Figure 2B for transect locations. +ve—positive value; +ve, contractional—positive values defined to be contractional (and negative ones, extensional); ± specifies 1 standard deviation of the measured quantity; N/A—not available. Strike is given as the azimuth (0–90°) of the NE end of the fault strike.
   *From Kearse et al. (2018) and T.A. Little (unpublished field data).
   †From Howell et al. (2020) and Kearse et al. (2018). Given as degrees clockwise from north for northwest side relative to "fixed" southeast side.
   §Based on linear intercept method applied to length of the transect: *S* = transect length / frequency.
   #Rotated fractures at this locality are shallow (0.3-m-deep) anthropogenic plough cuts rather than natural Riedel faults. For this reason, and because the dextral slip on the single splay analyzed at this transect site (3.5 m) is much less than for the other locations (5.8 m), fracture strike and zone width data from this site are not incorporated into the grand mean values (bold font, bottom rows).
   **In direction parallel to raft axes (= strike of R_{rot} faults). Original raft lengths (L_o) are calculated using the outer R angle (β_o), inner rupture zone width (W_{RI}), and the heave: $L_o = (W_{RI} + heave) / \sin(\beta_o)$.

because erosion since the earthquake has obliterated most of the original structures throughout the rupture zone. Where the fault traversed unconsolidated sand or gravel, the rupture trace was linear, narrow (<1.5 m wide), and lacking in obvious internal structure (Fig. 3A). In these narrow zones, finite shear strains were high (>5), and any early-formed structures were not preserved. In unconsolidated gravel or sand, fault throw was typically manifested by a simple scarp, inclined at the angle of repose of the faulted alluvium (see Kearse et al., 2018). By way of contrast, where the ground was underlain by cohesive soils developed on clay-rich sediments and covered in grass, more complex rupture zones featuring upraised mole tracks were characteristic (Fig. 3B). Prior to the 2016 earthquake, the walls of the paleoseismic trench in area C exposed a >4-m-thick upper layer of massive silty clay and clayey silt overlain by a <1-m-thick layer of peats and grass-matted topsoil (Little et al., 2018).

Rupture zones developed along subsidiary fault strands that experienced only minor (<1 m) slip indicate that all types of ground materials were initially deformed by en echelon arrays of once near-planar fractures (Fig. 3C). Most commonly, these were R faults arranged at a ~20°–25° clockwise strike angle relative to the main fault, each accruing a dextral-sense shear displacement. In some highly transtensive areas—for example, the pull-apart graben of area B in Figure 2B—primary extension fractures (F in Fig. 1C) developed in the rupture zone instead of R faults, while striking at a higher angle (~50°) to the main fault (Figs. 4A, 4B). In a field that was freshly plowed at the time of the earthquake (Fig. 2B, area D), the incised plow cuts broke up the clay-rich sediment into closely spaced, anthropogenic turf rafts that rotated clockwise during the earthquake (Fig. 3H).

The rest of this section will describe typical rupture zone structures developed on the grass-covered, clay-rich surficial materials that dominate the

Figure 3. Field photographs of the 2016 rupture trace on the Kekerengu fault. (A) Pure strike-slip rupture trace of the Kekerengu fault in unconsolidated beach sand at the coast (view to the southwest, 174.057°E, 41.973°S). Note the narrow, linear trace and lack of any preserved secondary structures. The furrowed morphology of the fault trace suggests some shear-related compaction of incohesive sand. (B) Up-bulged mole track along a minor trace (western part of area C, Fig. 2, 174.021°E, 41.972°S). Note the detached "turf rafts" separated by fissures. Rafts are subject to a combination of shear-related tectonic rotation and gravitational slumping. Photograph by Rob Zinke. (C) Synthetic Riedel (R) faults forming along a low-displacement splay of the Kekerengu fault where it cut across poorly sorted (silty) alluvium in the Kekerengu River. Splay is pure strike slip. Photograph, looking southwest (174.000°E, 41.979°S), by Nicola Litchfield. (D) Up-bulged mole track (174.031°E, 41.969°S), consisting of shortened turf raft bounded by rotated R faults. As the raft tears away, it leaves behind a scar that forms one wall of the gaping fissure between it and the adjacent raft. In the image, a raft in the original foreground was carried by strike slip to the left out of view, leaving only a raft scar behind. Photograph by Mark Hemphill-Haley. (E) Turf rafts and fissures on a strike-slip rupture that includes a vertical scarp (173.849°E, 42.070°S). The rotated turf rafts are semi-attached to the upper, more distant fault block, but unattached from the lower, closer one. The lower ends of the rafts have been displaced across the nearer block along a low-angle thrust flap. Note person in the background for scale. From Shag Bend on the Clarence River (to the west of Fig. 2). Photograph by Dougal Townsend. (F) Near-coastal mole track zone, looking northeast (174.024°E, 41.972°S). The fault is here uplifted on its northwestern side by ~1 m relative to the southeastern side. "Calving scars" are subparallel to the main fault trace or scarp, forming from tensile stresses at the scarp crest or slumping, whereas "raft scars" are bounded by R faults and form by tearing and tectonic rotation of turf strips. Narrower, more highly strained parts of the rupture zone have been disaggregated into an incoherent "mush" that is locally capped by isolated raft fragments. Drone photograph by Julian Thomson. (G) Detail of turf rolls along the thrust-faulted front of a turf raft (173.952°E, 42.002°S). Black and white arrow on card in the foreground is 10 cm long. Photograph by Mark Hemphill-Haley. (H) View toward the northeast toward Tirohanga lagoon and the coast, showing the Kekerengu fault trace cutting across a recently plowed field (174.047°E, 41.963°S). Northwestern side is here down-dropped relative to the southeastern side to form a scarp. The rupture zone has broken into narrow rafts bounded by deeply incised, vertical plow cuts. The rafts have rotated clockwise in proximity to the trace, while gaping fissures have opened up between the rafts.

Figure 4. Remotely piloted aerial vehicle–derived imagery of Kekerengu fault rupture zone for locations experiencing variably low to high slip and transtensional to transpressional motion. (A) Ground deformation along a low-slip (<1 m of dextral slip) fault strand in the Ben More pull-apart graben (area B, Fig. 2B). This transtensional locality ($\alpha = -33°$) provides a window into incipient structures in the rupture zone. These were mostly primary extension fissures (F), with subordinate Riedel (R) faults and a single Y (where Y fault denotes a fault that is subparallel to the main average fault trace) fault at the far left. (B) Another strand in the Ben More pull-apart graben—one that experienced ~7 m of dextral slip. Note the clockwise vertical-axis rotation of fissure (F)–bounded turf rafts in center of image (F_{rot}). On their left-hand side, these rafts transition into a much narrower Y fault. (C) Enlarged view of another part of the high-slip (~7 m) rupture segment in the Ben More pull-apart graben, showing a strongly rotated packet of turf rafts, each with intervening extension fissures. On both its left- and right-hand sides, the packet transitions along strike into a much narrower zone of Y faulting. (D) R fault–bounded turf rafts developed in a slightly transpressive ($\alpha = +5°$) part of the Kekerengu fault rupture (in area C, just to the east of transect 4; Fig. 2B). A low-slip fault strand near the top of the image preserves little-deformed R faults, whereas the higher-slip strand below it hosts slightly clockwise-rotated R faults (R_{rot}; note extensional gaping between them). Note how a large turf raft in the center left of the image has been partially broken up into sub-equant blocks by "2" structures (fractures cutting older R faults at a high angle) that cross-cut the older R faults. Displacement on the "2" faults includes sinistral (antithetic) shear offset and also extension.

landscape along the eastern Kekerengu fault. Most commonly, where the displacement vector was subparallel to the fault ($\alpha = 0°$ in Fig. 1C), the ground was broken into turf rafts bounded by en echelon Riedel (R) faults. These rafts developed at a mean width (or spacing, Fig. 1C) of 2–3 m. In the outer, little-deformed part of the rupture zone, which was typically 2–5 m wide, the R faults and their intervening turf rafts were little rotated. In many cases, individual R faults could be traced laterally into the adjacent inner high-strain zone, which was typically 1.5–4 m wide. Across this boundary, the R faults were deflected clockwise by as much as ~25°–30° to become R_{rot} faults. Between two adjacent R_{rot} faults, the intervening turf raft was deformed to form a pressure bulge. A contiguous series of such rafts formed an elongate deformational mound trending subparallel to the main fault trace (Figs. 3B, 3D). Rounded in profile, the mole tracks were raised an average of ~0.5 m above the surrounding (pre-deformational) ground surface (e.g., Fig. 5B, profile A-A'). This bulging records horizontal compression of the turf rafts. At some transpressional sites subject to large contractional heaves (e.g., the offset trench site in area C, subject to 1.3 m of heave), local bulge relief exceeded 1 m, but most of the deformational mounds were ~0.5 m high, showing no obvious correlation of mound height to local displacement angle (α). The shortened rafts alternated with between-raft fissures or depressions that were ~0.5–1.0 m deep and 0.3–1.5 m wide (Figs. 3D, 3E, 3H; Fig. 5B, profile B-B'). Where documented, strike-slip offsets on the R_{rot} faults were sinistral. We infer that during the earthquake, as turf rafts rotated clockwise, the rotated R faults along their margins widened into gaping fissures while also acquiring a sinistral offset. In many cases, lateral tearing-away of the deformed, grassy turf raft left a barren-earth scar at its site of origin in the outer rupture zone. We refer to these as "raft scars" (Figs. 3D, 3F). The structural depressions that opened up between the
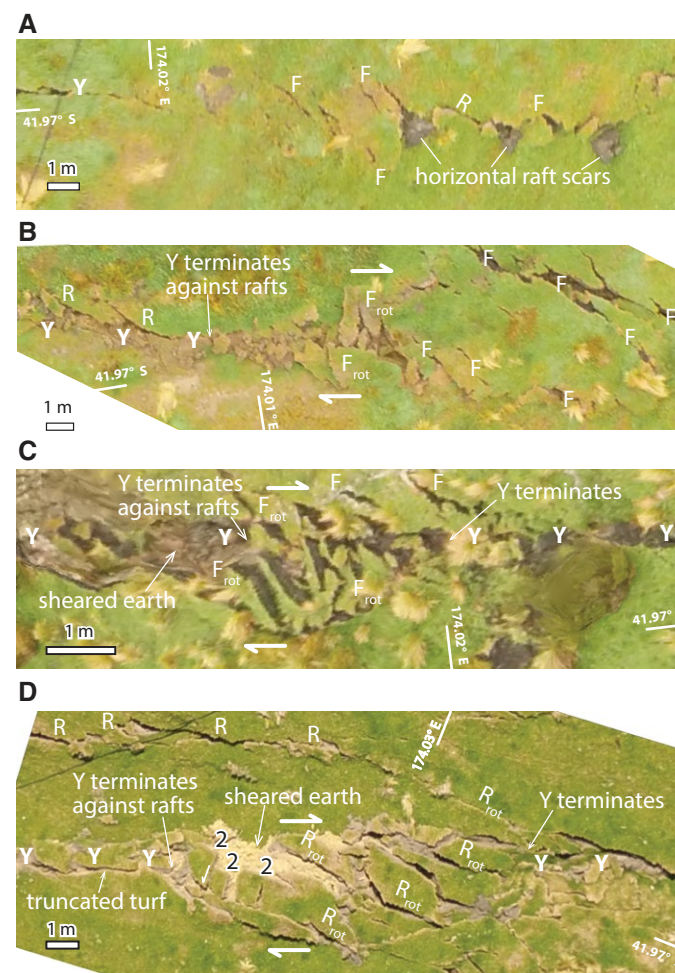
rotated turf rafts were quickly infilled with broken clods of earth and water, making it difficult to measure their original depth. Some raft scars probably marked the trailing edges of fault slices that were translated away laterally (rather than rotated)—presumably dextrally—to reach a final resting place perhaps many meters away (Fig. 3D).

In some places, the rupture zone of the Kekerengu fault was broken by one or more scarps. Most commonly 0.3–1.0 m high and locally as much as ~2 m high, these scarps introduced gravitational stresses promoting the collapse or toppling of the upraised block. The downward tearing-away of turf rafts under gravity resulted in localized opening of extensional fractures along their upper margins—structures that we here refer to as "calving scars" by analogy

Figure 5. Example of structural interpretation along a strike-slip part of the 2016 Kekerengu fault rupture at transect 1 of area C (Fig. 2B); figure shows the westernmost ~45 m of the 57-m-long transect. This area experienced a displacement that was parallel to the local fault strike. The rupture zone here accommodated ~8.9 m of dextral slip and ~0.1 m of northwest-side-up throw. (A) Orthophotograph without interpretation. Inset area in the white box provides an enlarged view of the western part of the rupture, with interpreted fracture types labeled according to the scheme in Figure 1C. (B) Topographical profiles transverse (A-A') and parallel (B-B') to the strike of the rupture zone, taken from the digital surface model that was derived from processing of the aerial images. Note deformational bulges and fissures. (C) Same orthophotograph overlain by structural interpretation (structural symbols are the same as in Fig. 6). (D) Structural interpretation without the photographic base. (E) Enlarged view (uninterpreted) of strongly clockwise-rotated "turf raft." (F) Interpreted internal structure of the turf raft, with "2" faults displacing the older, R fault–bounded margins of the raft with extension and sinistral strike slip. The southern margin of the packet of strongly rotated rafts overthrusts the southern block (blue line).

with icebergs (Figs. 3E, 3F). In contrast to raft scars, which strike parallel to R faults, calving scars strike subparallel to the main fault trace. Individual turf rafts may be bounded by both types of features (raft scars and calving scars) along different sections of their perimeter. We note that not all calving scars necessarily represent slope-driven gravitational failures. Some are probably of tectonic origin, developing as a result of fissuring at the crest of a monoclinal scarp flexure, by lateral tearing-away of the end of a turf raft during tectonic rotation of its limb, or because the raft was eventually translated by a Y-type strike-slip fault during the earthquake.

The inner high-strain zones commonly displayed an across-strike asymmetry. On one side, the ends of rotated turf rafts remained semi-attached to their less-rotated continuations in the outer rupture zone, from which individual R faults could be tracked, with varying degrees of continuity, into the inner high-strain zone, where they were more clockwise striking (R_{rot} faults). On the opposite side of the inner zone, the turf rafts were faulted (Figs. 1C, 3E). Along this margin, slip on a throughgoing oblique thrust, striking subparallel to the main fault, emplaced the mass of deformed rafts outwardly over little-deformed ground of the outer rupture zone. We refer to the first type of boundary as an "attached" side, and the second type as an "unattached" one (Figs. 1C, 3E). Where the fault zone was broken by a topographic scarp, the attached side of the inner rupture zone typically formed along the upper scarp slope, whereas the unattached side occupied the base of slope on the downthrown side (Fig. 3E). Where a scarp was absent (e.g., pure strike-slip strand), this asymmetry did not always exist; for example, some mole tracks were unattached on both sides. In the latter case, both margins of a mole track were thrust outward over undeformed ground in opposite directions along a pair of low-angle faults that dipped inwardly beneath the uplifted mass of mole track. Evidence for internal contraction of the turf rafts and for their thrust emplacement across adjacent less deformed ground included: (1) mounding or folding of grass-covered topsoil (Figs. 3B, 3D, 3G); (2) turf rolls along the outer margins of the rafts (Fig. 3D); and (3) thrust wedges of deformed earth overriding the grass-covered, pre-earthquake ground surface (Fig. 3G).
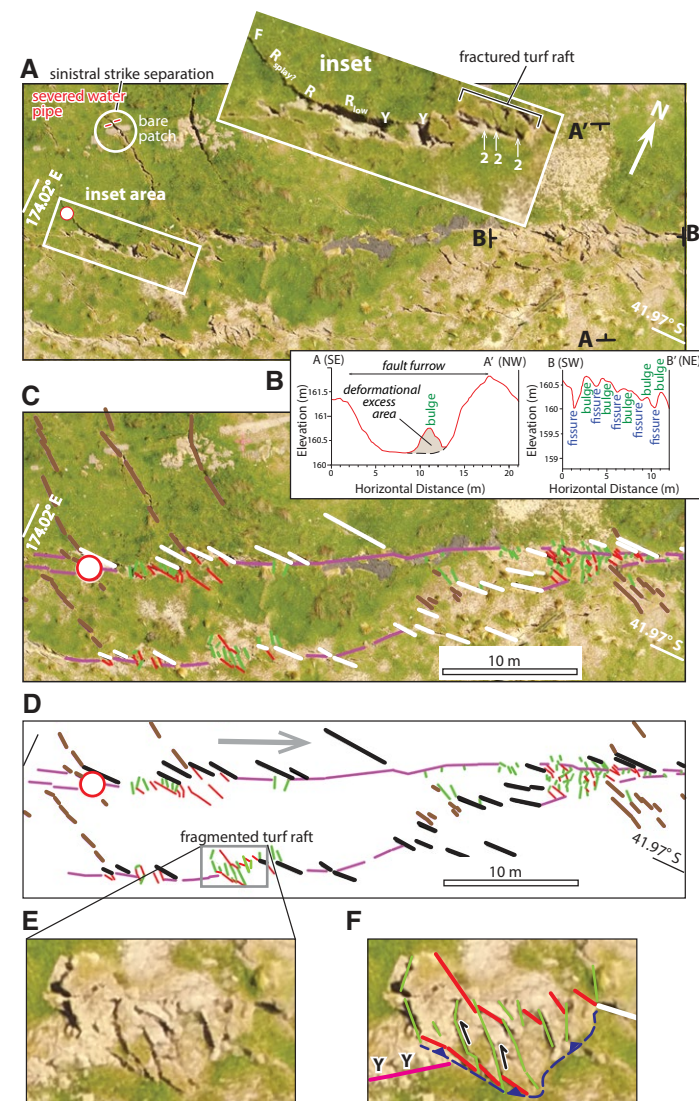
■ HIGHLY SHEARED ZONES

Where the Kekerengu fault accommodated 8–12 m of dextral-slip, the internal structure of its inner rupture zone was complex, even chaotic. Where individual rafts could be traced entering the high-strain zone at its boundary with the outer rupture zone, they generally could not be traced vary far. By

studying fault strands that accrued only minor slip, one can interpret how high-displacement sites might have appeared at an early stage of their development. In such sites, turf rafts could be observed fragmenting into blocks as a result of their transection by secondary fractures (labeled "2" in Fig. 1C) that strike at a high angle (~70°–95°) to the main fault trace (e.g., Fig. 4D). Rotated Riedel faults (R_{rot}) were commonly cut and offset by these secondary fractures, which were clearly younger (Figs. 4D, 5D, 5E, 5F). Where shear offsets were recognizable on the secondary fractures, they were consistently sinistral. In addition, the secondary fractures also experienced an extensional opening. At high-displacement sites, the rupture zone typically contained one or more Y-oriented corridors of highly sheared earth. In these corridors, fragmented blocks of grassy turf raft were dispersed in a matrix of barren earth and widely separated from one another. The secondary fractures that cut and/ or bounded these blocks typically strike 30°–50° clockwise of the older R_{rot} faults (e.g., Fig. 5A inset; Figs. 5E, 5F). It is difficult to assess how much the secondary fractures may have rotated during the ground deformation, and thus what their strikes may have been at inception. Nor is it obvious whether any less-rotated equivalents to the secondary fractures were preserved in the outer rupture zone. Gaping extensional fissures (F) are one candidate for such precursors (brown lines in Figs. 5C, 5D). These were most common in the outer fringes of the rupture zones, where they typically strike 25°–30° clockwise of nearby (unrotated) R faults, that is, some 50°–60° clockwise of the main fault trace. One of them severed a water pipe and adjacent patch of bare ground (Fig. 5A, inside white circle) with a sinistral sense of strike separation. The offset largely reflects extensional opening across the fissure but may include a small shear displacement.

In the inner rupture zone, grass-covered turf-raft fragments were commonly mixed into a soft matrix of sheared earth (e.g., Figs. 4C, 4D). Based on the known dextral displacement (8–11 m) and widths of the matrix (0.4–2.0 m), we infer finite shear strains (γ) in the sheared matrix of >4, locally reaching as high as ~24. The Y-striking corridors of sheared earth sharply truncate grassy turf along their margins and are the surface expression of high-slip strike-slip faults. A commonly observed relationship was the following: A Y fault would terminate laterally against a deformed mass of rotated turf rafts, while "reappearing" along strike on the opposite side of that mass (e.g., Figs. 4C, 4D, 5D, 5F). From this relationship, we infer that the Y faults were continuous at depth, but in the near surface they terminated upward against the detached mass of rafts—while breaching the surface on either side of the mass.

■ THICKNESS OF THE MOLE TRACKS

How thick was the deformed mass (grassy turf and clay-rich sediment separated by fissures) that became bulged up into the mole track?; i.e., at what depth did it detach from underlying material? One can use area-balancing methods on profiles parallel to the long axes of the rafts to estimate a mean "depth to detachment" for the rafts:
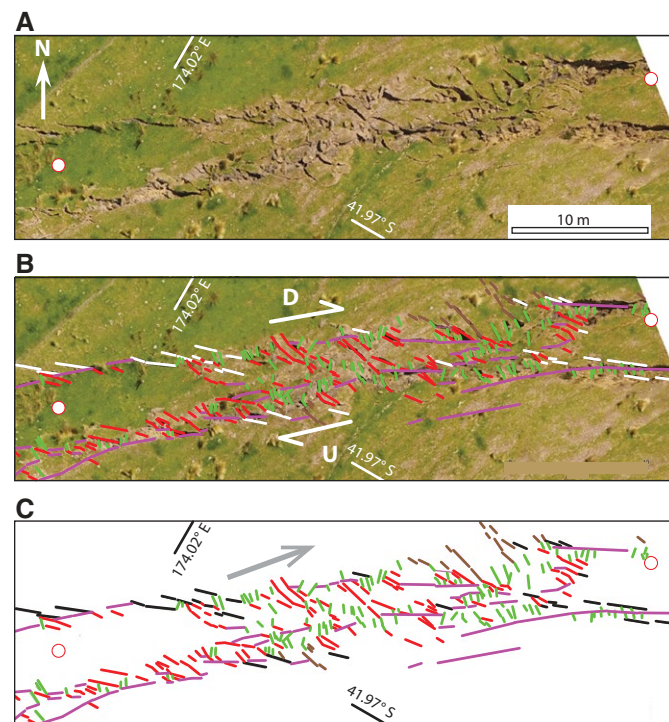
$$d = A/\Delta s, \tag{1}$$

where d is the depth to detachment, A is the deformational excess area of the bulge (area of the bulge protruding above the inferred pre-deformational ground surface measured on a profile of the DSM), and Δs is the axial raft shortening (in meters), as calculated using the deformable slat model (see below, and Item S2 [footnote 1]). Using this model, the shortening (Δs) can be calculated from (1) the mean strikes of Riedel faults outside (R) versus inside (R_{rot}) an inner rupture zone and (2) the width of the zone. Morris (2020) undertook such a calculation along the length of area C (Fig. 2B), averaging the excess area (A) that was observed in 28 topographical profiles. Her average value for A was 1.6 ± 1.3 m^2 (1σ) and for Δs was 2.4 ± 0.9 m. Using Equation 1 to solve for the depth (d), these data imply a mean detachment depth for the rafts of 0.7 ± 0.6 m. The standard deviations of A and Δs are large, hence the large relative uncertainty in the mean detachment depth derived from those estimates. The depth (d) is greater than the thickness of the near-surface root mat, which is typically <0.15 m, implying that the integrity and thickness of the turf rafts was not controlled by the maximum depth of grass roots, but by the clay-rich material underlying them. Variability in detachment depth is not unexpected considering (1) the lateral variability in kinematics (transpression, transtension, pure strike slip) between different parts of area C and (2) the likely along-strike variability in thickness and nature of near-surface sediments in that region.

The above estimate for raft thickness or detachment depth—at ~1 m—is consistent with field observations. Rapidly infilled with collapsed debris, the gaping fissures that occurred between the adjacent rotated rafts were found to be as much as ~1 m deep, suggesting a raft thickness at least this large. In a few places, patches of barren ground could be matched to nearby turf rafts that had clearly been torn away from these patches during their rotation. These were essentially horizontal raft scars, and their shallow recessed depth indicates that these rafts were only a few decimeters thick at their base and that their uncoupling depth was probably controlled chiefly by the thickness of the grass roots layer (Fig. 4A). Generally, however, the rafts of detached near-surface material had a side-on exposed thickness of >0.5–0.75 m (e.g., Fig. 3G), indicating a thickness in excess of that.

■ STRUCTURAL MAPS OF THE RUPTURE ZONE

We used the RPAS-derived orthophotographs as a base on which to plot a structural interpretation of the rupture zone on seven transects in areas A, C, and D (Fig. 2B). The exact location of the transect end points are given in the Supplemental Material (Item S2 [footnote 1]). Several examples of structural maps are provided in Figures 5, 6, and 7. In particular, these show our interpretation of transects 1, 2, and 4 in area C. On each transect, the Kekerengu fault has a different local strike. Together, the three localities represent a case of pure strike slip ($\alpha = 0°$), one of slight transtension ($\alpha = -12°$), and one of
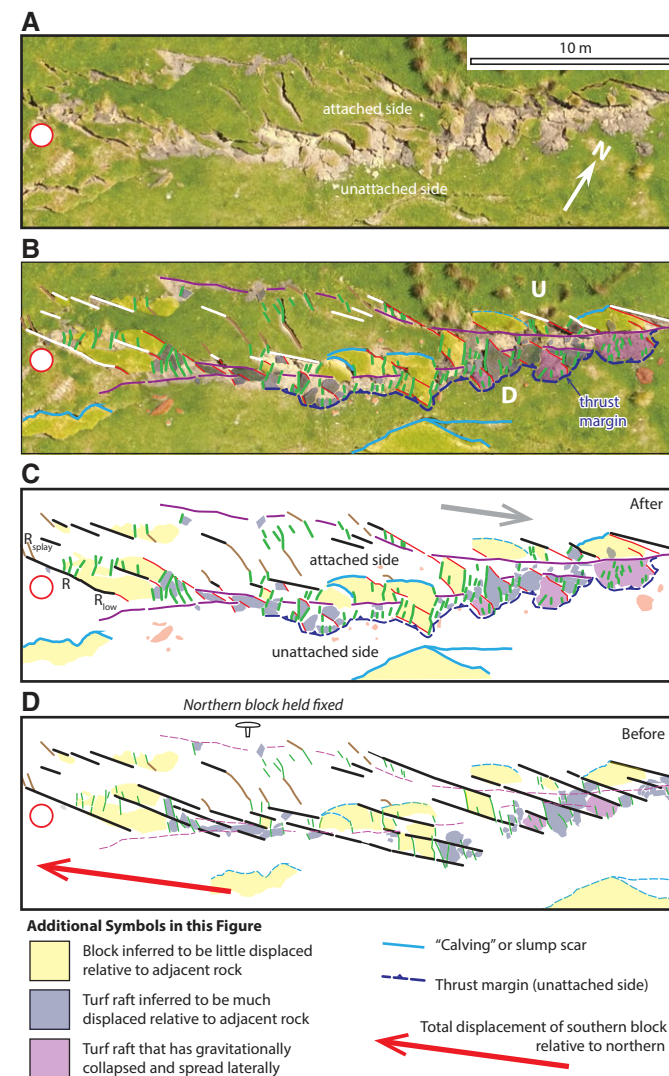
Figure 6. Example of structural interpretation along a transtensive part of the 2016 Kekerengu fault rupture at transect 4 of area C (Fig. 2B); image shows the entire 44-m-long transect. This area experienced a (northwest side relative to southeast) displacement that was 12° anticlockwise from the local fault strike. The rupture zone here accommodated ~8.0 m of dextral slip and ~0.6 m of northwest-side-down throw. (A) Orthophotograph without interpretation. (B) Same orthophotograph overlain by structural interpretation. (C) Structural interpretation without the photographic base.

Explanation

○ Transect end point

— Synthetic Riedel (R) fault (interpreted as unrotated, shown white in panel B)

— Extension fissure (F, interpreted as little rotated)

— Deformed synthetic Riedel (R) fault (interpreted as clockwise rotated)

| Secondary fracture ("2")—either primary extension fissure or antithetic Riedel fault. (now with sinistral offset and opening, and interpreted as clockwise rotated).

— Dextral slip fault (Y, subparallel to main strike of rupture); also includes some "calving scars"

➤ Trend of fault displacement (NW side relative to "fixed" SE side)

Figure 7. Example of structural interpretation along a transpressional part of the 2016 Kekerengu rupture at transect 2 of study area C (Fig. 2B); figure shows the westernmost ~35 m of the 115-m-long transect. This area experienced a (northwest side relative to southeast) displacement that was 8° clockwise from the local fault strike. The rupture zone here accommodated ~9.0 m of dextral slip and ~1.0 m of northwest-side-up throw. (A) Orthophotograph without interpretation. (B) Same orthophotograph overlain by structural interpretation (structural symbols the same as in Fig. 6 or as indicated in the key at the bottom). (C) Structural interpretation without the photographic base (Fig. 1C). (D) Schematic retrodeformed model of the ground prior to the earthquake, showing possible original locations and attitudes of deformed turf rafts and fractures depicted in C.

Additional Symbols in this Figure

▢ Block inferred to be little displaced relative to adjacent rock

▢ Turf raft inferred to be much displaced relative to adjacent rock

▢ Turf raft that has gravitationally collapsed and spread laterally

— "Calving" or slump scar

- - - Thrust margin (unattached side)

➤ Total displacement of southern block relative to northern

slight transpression (α = +8°). The Supplemental Material (Items S3A–S3G [footnote 1]) presents a full set of structural maps for all of the transects. In these maps, fault and fracture traces are color coded (see Figs. 1C and 6 for color scheme) to represent our interpretation of fracture identity (e.g., as R, R_{rot}, "2", F, or Y). For each fault-parallel transect, the strike of every structure was digitized, and the rupture zone widths W_{RI} and W_{RT} were measured at a spacing of 1–2 m. In addition, the mean spacing of R fractures for each transect was measured using the linear intercept method. Especially in the highly strained, inner part of the rupture zone, where the rafts were commonly discontinuous or broken up, attribution of fracture identity was commonly subjective, so our interpretations are not unique. A recurrent uncertainty was assessing how strongly rotated a fracture was at particular points in an image, how it might be correlated to other, less-deformed structures in the outer rupture zone, and how the intensity of deformation varied with distance away from that point.

Figure 7 illustrates many of the features described above. It shows an inner rupture zone that is semi-attached on the upthrown side of the fault along the top of the image ("attached side"), where the turf rafts were little displaced relative to the scars from which they appear to have been sourced. On the opposite ("unattached") side of the main fault, the same rafts are emplaced along a "thrust margin." This map exemplifies the tendency for the center of the rupture zone to be cut by two closely spaced Y fault strands (purple traces), with most of the rotated turf rafts occupying the corridor between these two faults (see also Figs. 5 and 6). Outside of the two Y faults, raft and calving scars are present and the Riedel (R) faults appear little rotated. Some fissures (F) in the outer region seem to have propagated at an acute clockwise angle away from the extensional tips of Riedel faults in a geometry reminiscent of wing cracks or R_{splay} faults of Naylor et al. (1986). This relationship is also expressed in Figure 5A (inset), as are R faults that curved toward Y faults in a geometry reminiscent of R_{low} faults (Fig. 1C).

The maps (Figs. 5, 6, and 7; Supplemental Material, Item S3 [footnote 1]) reveal that the secondary ("2") fractures (green colored traces in the figures) are shorter and much more numerous than the (combined) R + R_{rot} faults (Figs. 5D, 6C, and 7C). Such relationships are geometrically anticipated because the secondary fractures caused a cross-fragmentation of the preexisting R fault–bounded turf rafts. Taken to an extreme, the raft fragmentation process yields scattered blocks of turf surrounded by sheared earth.

A summary of our digitized measurements at each transect site is presented in Table 1. Key results include: (1) the rupture zone varied in strike between 062 and 082, whereas the displacement azimuth varied in local convergence angle (α) between +8° (transpressional) and –12° (transtensive) while being close to 0° (pure strike slip) on average; (2) the rupture zone averaged 6.2 ± 2.2 m in total width (grand average ±1σ for the seven sites), whereas the inner, high-strain sub-width of that zone averaged 2.8 ± 1.4 m; (3) in the outer rupture zone, R faults on average strike 25° ± 3° clockwise of the main fault (angle β in Fig. 1C), whereas in the inner rupture zone, the mean strike of the rotated R faults (R_{rot}) increased to 52° ± 9°; (4) in the inner zone, the secondary ("2") fractures strike at 90° ± 6° on average to the main fault; and (5) in the outer

zone, the gaping fissures (F) on average strike at 53° ± 6° to the main fault. The average vertical relief of deformational bulges was 0.5 ± 0.1 m, whereas the average horizontal shortening causing this relief, as calculated from area balancing parallel to raft axes, was 1.6 ± 0.8 m.

■ KINEMATIC MODELS FOR GROUND DEFORMATION IN STRIKE-SLIP RUPTURE ZONES

The simple shear approximation has been widely applied to describe how strike slip on a fault at depth may be distributed through a wider zone of sheared materials in the near surface. In a case of pure strike-slip shearing, both the length and width of the deforming zone are constant and surface area is conserved (e.g., Wilcox et al., 1973). A more complex type of homogeneous deformation, ideal transpression, was introduced by Sanderson and Marchini (1984) to describe shearing in a constant-volume deformation zone, vertical in dip, that has a fixed strike length but a variable width. Here, the displacement angle (α) is allowed to be nonzero, and any fault-orthogonal motion (heave) is balanced by vertical stretching (i.e., up-bulging; Fig. 8A) to maintain volume. For a specified displacement angle (α) and magnitude, the model predicts the orientation and magnitude of the finite strain ellipsoid in the deformed zone and the length changes and angular rotation of passive markers of any specified orientation. The distortional rotation of a marker is the difference between its original (or outer) angle β_o and its final (inner) angle β_i (Fig. 8B). In a transpressive dextral shear zone, most markers rotate clockwise, while the axis of principal stretching achieves a decreasing acute angle to the zone boundary as displacement increases. If α = 0° (end-member case of strike-slip simple shear), all markers that are backward inclined relative to the shearing direction (e.g., R faults or turf rafts) are predicted to be shortened initially, whereas all forward-inclined ones (e.g., poles to the R faults) are predicted to be steadily extended. Note that the particular lines that end up rotating into exact perpendicularity with the strike of the zone ("final fault-perpendicular direction," β_i = 90) are predicted to be shortened despite the shear zone itself experiencing no net convergence or width change in that same direction.

An alternate model, variously called the "bookshelf," "domino," or "slat" model, accommodates distributed shearing by a rotational type of discontinuous and heterogeneous deformation (e.g., Terres and Sylvester, 1981; Nur et al., 1986; Mandl, 1987). In its simplest form, the model invokes the vertical-axis rotation of rigid slats (clockwise for a dextral shear zone). The fixed length of the rigid slats requires the strike-perpendicular width of the deformation zone to change as the slats rotate with increasing displacement. For a given slat rotation (β_o to β_i), the shear displacement and change in width of the deforming zone are geometrically determined, as is the displacement angle α, which cannot be imposed independently. If the slats (or in our case, turf rafts) are not rigid, but are allowed to shorten internally (or thrust outward) as they rotate (in order to fit inside a deforming zone of specified width), then the slat model must be modified to accommodate this deformation, a
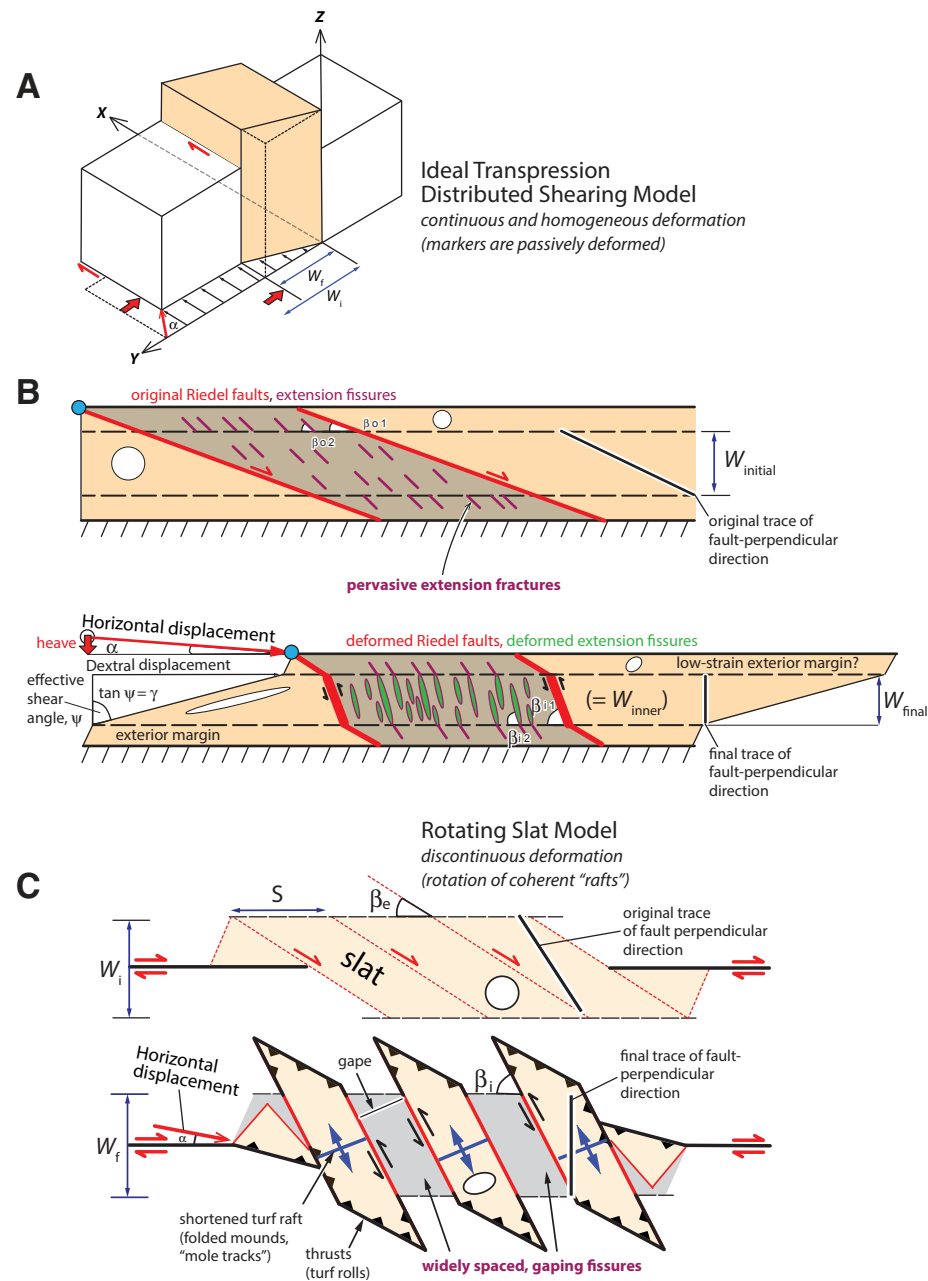
Figure 8. Cartoons illustrating two end-member kinematic models for rupture zone deformation, both of which prescribe no length changes parallel to the strike of the zone. (A) Three-dimensional block diagram illustrating the concept of "ideal transpression" (after Sanderson and Marchini, 1984). The deformed volume (shaded) has vertical boundaries along the X-Y plane. It is homogeneously and continuously deformed as a result of shearing parallel to the fault strike direction (x-axis) together with a component of fault-orthogonal convergence. The latter reduces the width of the zone from W_i (initial) to W_f (final) and causes its thickening and vertical uplift (where α is angle between the fault strike and the local displacement vector). (B) "Ideal transpression" model: Upper cartoon is a plan view of the undeformed state. Several passive markers are shown, including incipient Riedel faults (red, originally striking at $β_{o1}$ to the fault), extension fissures (purple, originally striking at $β_{o2}$), and original circles (future strain ellipses). Lower cartoon depicts the corresponding deformed state, here depicting two exterior margins that experienced low strain and an inner zone that experienced high strain. In the deformed state, the Riedel faults and fissures have been rotated to strike angles $β_{i1}$ and $β_{i2}$ in the inner zone, respectively, and to smaller angles (not labeled) in the two outer zones. The circles are now strain ellipses. (C) "Rotating slat" model: Upper cartoon is a plan view of the undeformed state. Incipient Riedel faults (red, originally striking at $β_e$ to the fault) bound coherent "turf rafts." Lower cartoon depicts the corresponding deformed state. Riedel faults have been rotated to new strike angle $β_i$ and are now separated from one another by wide, gaping fissures. The rafts are thrust outward over adjacent undeformed ground, or internally shortened along their axis and vertically thickened, or both.

Little et al. | Evolution of mole tracks

change that allows the shear displacement and the displacement angle (α) to be independent parameters. We refer to this modification of the rotated slat model (Fig. 8C) as the deformable slat model. Using this model, if the displacement angle (α) is known *a priori*, and the rotation path of R fault–bounded turf rafts can be tracked between their initial strike angle, β_o, to their final strike angle, β_i, then not only can the overall shear displacement accommodated by this slat rotation be calculated, but also the necessary internal shortening (deformation) of the raft parallel to its length. In this model, the direction (*Z*) of the minimum finite principal stretch ($1 + e_3$ [where e_3 is the smallest (most negative) longitudinal strain]) is parallel to the raft axis. In addition, one can calculate the (lesser) shortening experienced by any other material line in a raft, as specified by its final orientation, for example, one that ends up exactly perpendicular to the strike of the deformation zone at the close of deformation. The final fault-perpendicular direction is generally oblique to the long axis of the raft (Fig. 8C). As the slats shorten, they must structurally thicken to maintain volume; moreover, increasing space (gaping fissures) must open up between adjacent slats as they rotate. If we ignore deformation-induced porosity changes (these are probably small dilatations compared to other strains), neither the area nor volume of the shear zone as a whole changes as a result of this deformational redistribution of material. The Supplemental Material (Items S4A and S4B [footnote 1]) presents the geometry of the deformable slat model, trigonometrically relating the rotation-accommodated displacement and its angle, α, to changes in slat strikes across the zone (from β_o on the exterior to β_i in the interior). It also calculates the required shortening of the rotated slats parallel to their length and the shortening of the particular line (interior to these slats) that ends up orthogonal to the strike of the shear zone.

■ DISCUSSION

Effects of Ground Material and Boundary Conditions on Mole Track Development

During slip in the 2016 Kaikōura earthquake, the structural response of the ground to large strike-slip displacements on the Kekerengu fault was variable. Unconsolidated surficial sediments (beach sand, alluvial gravel) typically broke in a single, narrow (<1.5-m-wide), almost linear zone at the surface without the development of "push-ups" (mole tracks) or long-lived Riedel faults (Kearse et al., 2018). Elsewhere, the landscape was typically underlain by a >1-m-thick layer of clay- and silt-rich (partly loess-derived) sediment and topsoil, capped by a tightly interwoven mat of (mostly nonnative) grasses. The latter layer contributed to cohesion of the turf rafts but generally did not control their thickness, whereas the former typically did not uncouple along bedrock or any obviously harder layer below. In these locations, the rupture zone was typically >5 m wide and was broken and segmented by regularly spaced Riedel faults into turf rafts. Vertical-axis rotation of these rafts accommodated

some of the coseismic strike slip, a slat-like distributed deformation that was accompanied by internal shortening and bulging of serially arranged turf rafts that amalgamated along strike to form an elongate array of "mole tracks." The above-described contrast in surface expression between different materials (unconsolidated sand or gravel versus clay-rich rafts) is anticipated by analogue modeling studies of strike slip at depth below an originally undeformed cover layer (the so-called "Riedel" boundary condition). Dry sand, which is nearly cohesionless and which tends to strain weaken, tends to host long, well-connected, relatively high-slip faults, whereas clay, which is cohesive, tends (depending on its water content and dilatancy) to strain harden and spread deformation across a wider zone containing numerous shorter and less well-connected faults (e.g., Dooley and Schreurs, 2012). Moreover, wet clay and silt (largely derived from loess) are prone to both folding and extension fracturing—both of which are key attributes of the natural rupture zones described in this paper.

Seismological and geodetic data indicate that the Kaikōura earthquake ruptures propagated northeastward into our study region at the northeastern end of the Kekerengu fault (Hamling et al., 2017; Kaiser et al., 2017; Ando and Kaneko, 2018), the part of the fault that yielded the greatest slip and moment release during the earthquake (Cesca et al., 2017; Kearse et al., 2018; Howell et al., 2020). What were the boundary conditions applicable to this dynamic rupture propagation, and how might they have influenced structures developed in the near surface? Analogue modeling studies, elastoplastic dislocation strain modeling, analogue deformation experiments based on the Riedel boundary condition (a mode III dislocation type of boundary condition), and linear elastic fracture mechanics–based studies of mode III crack propagation all generally predict a linear, almost 1:1 scaling relationship between cover thickness and the width of the characteristically segmented zone of brittle or plastic deformation (i.e., Riedel faults) that develops ahead of the buried fracture (Naylor et al., 1986; Bowman et al., 2003; Dooley and Schreurs, 2012; Cambonie et al., 2018). Along the Kekerengu fault, the characteristic narrowness of the surface rupture zone (~4–8 m) and its widespread segmentation into obliquely striking Riedel faults suggest an upward, mode III rupture propagation. This is because if the upper tip line of a slipping planar dislocation is buried only a few meters below the ground surface, then—by analogy with the "Riedel" experiments—any intact materials above that tip line should experience a distributed shearing in a deformed zone that is of similar width to the dislocation depth; moreover, the greatest principal stress (σ_1) in that zone should be arranged at ~45° to the fault trace, which is a disposition that would promote "ideal" attitudes of Riedel faults. In reality, however, the rupture front was probably mixed mode (combination of modes II and III); that is, it was oblique to the surface rather than purely mode III and horizontal. Because ruptures propagate faster at depth than they do at the surface, a rupture front that propagates unilaterally in map view would develop a 3-D tip line that is neither vertical nor horizontal. When it arrives at the surface, its tip line would most likely be gently inclined from the horizontal, carrying a dominance of mode III deformation relative to mode II. We interpret the narrow, segmented character of the rupture zone

of the Kekerengu fault to indicate that the dislocation at shallow depth was dominated by mode III at the time when the mole tracks formed (Kearse et al., 2019). The early increment of rotational ground deformation presumably took place prior to full breaching of the rupture, when the "effective" depth of the dislocation was <10 m deep. We note, however, that the width of surface rupturing was probably also influenced by the cumulative effects of previous ruptures at the site, with preexisting shear bands, for example, potentially contributing to a narrower deformation zone in the near surface (Oettle and Bray, 2013). Clearly, the issue of dynamic boundary conditions is complex.

Finite Evolution of the Strike Slip–Dominated Rupture Zone

Based on our observations, we suggest a model for the progressive deformation of cohesive, near-surface materials in a large-displacement strike-slip rupture zone. Area B in our Kekerengu fault study area (Fig. 2B) provides a simple visual illustration of the model. Here, a ~300-m-wide pull-apart graben hosted a dense array of subparallel faults subject to variably small (<1 m) to large (~7 m) displacements (Kearse et al., 2018). The images in Figures 4A–4C depict a progression of ground deformation as a result of variably small to large, slightly transtensive dextral slip as expressed on different fault strands. The progression involved: (1) formation of an oblique fracture array (in this case mostly gaping extensional fissures; Fig. 4A); (2) localized rotation of "packets" of shallowly detached turf rafts surrounded on both sides—and presumably also at depth—by discrete strike-slip faults (Y faults; Fig. 4B); and (3) further rotation with widening of the intervening fissures, which acquire an antithetic shear displacement, and internal fragmentation of the rafts with local development of highly sheared earth (Fig. 4C). The example is especially simple for two reasons: (1) the unusually transtensive direction of displacement ($\alpha \sim -33°$) at this site obviated the need for the turf rafts to shorten or bulge upward; and (2) most of the host fractures formed as extensional fissures striking at a ~50° primary angle to the main fault trend. Such a large strike angle promoted the vorticity-induced vertical-axis rotation of the turf rafts while further reducing their requirement for axial compression. Preferred (or easy) rotation of antithetic-slipping fractures striking at a high angle to the strike-slip zone has been observed in both nature and experiment (e.g., Wilcox et al., 1973; Terres and Sylvester, 1981; Schreurs, 1994) and is explained mechanically by Mandl (1987). Area D (transect 1), located in recently plowed ground along a fault strand that accrued only ~3.5 m of slip during the earthquake, provides another example of rupture-zone expression at a low strike-slip magnitude (see Supplemental Material, Item S3G [footnote 1])—though a case where the rotating fractures (and rafts) were anthropogenically imposed.

In naturally deforming strike slip–dominated locations, ground deformation initiates with the formation of Riedel (R) fault arrays (Fig. 9). These strike at a lower angle to the main fault trace than do fissures (F), and they initially acquire a synthetic sense of strike slip with push-up structures near their tips. As the turf rafts rotate, they become increasingly separated from one another

by fissures that begin to acquire an antithetic-sense shear offset. The rafts are also strongly shortened to form up-bulged mounds and are detached on one or both sides by flap-like contractional faults along which the mole tracks are outwardly emplaced across the little-deformed outer rupture zone. After their rotation has accommodated a strike-slip displacement of ~3–4 m, the rafts become internally fragmented by numerous secondary ("2") fractures that strike at a high angle to the main fault trace. The resultant turf blocks become scattered in the strongly sheared earth of the inner rupture zone, in which they are further translated and variably rotated. The rest of the displacement accumulates discretely on one or more of the Y faults that cut the interior and/or outer margins of the inner rupture zone. Figure 7D shows a somewhat ambitious attempt to retrodeform the map of Figure 7C in accordance with the above model.

An enigmatic aspect of the above scenario is the origin of the secondary ("2") fractures and the path by which they ultimately acquired a mixture of antithetic strike slip and extensional opening. Did they begin as extensional fissures (F) but were later rotated to acquire a later antithetic shear offset? Or did they initiate as antithetic Riedel (R′) faults, perhaps originally striking at ~70°–80° to the main fault trace, while acquiring the extensional displacement later?

An observation relevant to this question is the following: at 35°–40° (Table 1), the mean angular difference in strike between fissures (F) in the outer rupture zone and secondary fractures ("2") in the inner one is greater than the mean deformational rotation of the Riedel faults (25°–30°). Because the secondary ("2") fractures cross-cut older R faults and ended up approximately orthogonal to the main fault, the above angular shortfall implies that the secondary fractures initiated at an originally high angle to the main fault trace, perhaps 70°–80°, while undergoing only a minor clockwise rotation after that. On this basis, we prefer the interpretation that the secondary ("2") fractures began as antithetic Riedel (R′) faults, after which they experienced an average clockwise rotation of only ~10°–20°.

In both nature and experiment, R′ faults are not consistently developed in strike-slip zones. Experimental conditions favoring their formation include: (1) suppressed lateral confinement (e.g., Schreurs, 1994); (2) the presence of a cohesive and/or thick upper layer (e.g., clay; Atmaoui et al., 2006); and/or (3) a distributed shear boundary condition imposed at the base of the upper, unfaulted layer (i.e., no discrete basement discontinuity; e.g., Schreurs, 2003; Dooley and Schreurs, 2012). The latter condition leads to short R′ faults cutting (and linking) between earlier-formed, longer R faults. Of these proposed conditions, the last two seem most relevant to our natural example. After the R fault–bounded blocks of ground became vertically detached into rafts, perhaps continuing shear beneath them imposed a distributed shear traction at their base, thus promoting a late onset of R′ faulting.

Which end-member kinematic model (Fig. 8) does a better job of describing how the ground deformed during the large strike-slip displacement on the Kekerengu fault in 2016? Our observations suggest that the deformable slat model can best approximate the kinematics of ground deformation during early stages of the coseismic displacement when the turf rafts were isolated
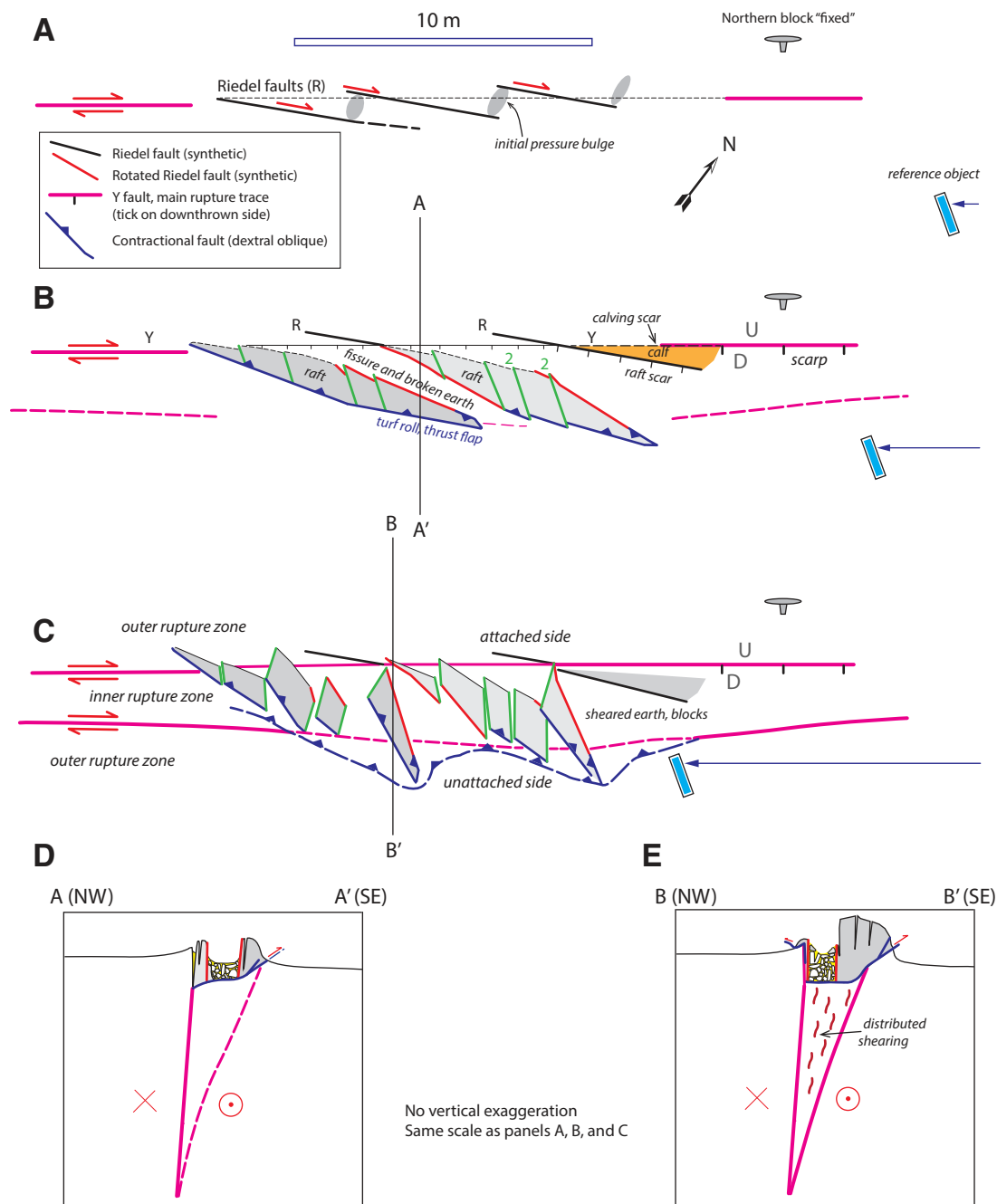
Figure 9. Cartoon illustrating the proposed structural evolution of ground deformation during a large strike-slip (~10 m slip) earthquake rupture. Northern block is shown "fixed." Slip of the southern block is indicated by motion of a cartoon water trough ("reference object"). (A) Incipient rupture: Riedel faults nucleate and slip dextrally. (B) Later snapshot, showing breakage of the ground into "turf rafts" that have rotated clockwise as a coherent mass while separating from one another along steep-sided fissures infilled with broken material derived from the rafts. "Raft scars" mark the original location of raft margins that were subsequently torn away. The rafts are relatively pinned to one fault block (the "attached side," here depicted as the northern block), but "unattached" from the other, above which they are thrust outward along a low-angle contractional fault. The rafts quickly fragment into smaller, more equant blocks by development of secondary fractures ("2"), interpreted as original conjugate Riedel faults. Other turf blocks ("calves") form by gravitational failure or toppling of the rising scarp along fractures subparallel to the main fault trace. These blocks may not rotate. (C) After large slip, the rupture zone is pulverized, and any remaining intact raft blocks are scattered and differentially rotated, a final deformation that we attribute to distributed shearing beneath them. This shearing further separates the block remnants from one another. In addition, throughgoing discrete faults (Y shears) form and link together. Commonly these occur on both flanks of the strongly disturbed rupture zone. (C and D) schematic cross-sections A-A′ and B-B′ for panels B and C, respectively.

by R faults and rotated clockwise. Initially dextral, the R faults later acquired sinistral shear offsets and their walls opened up into gaping fissures. The up-bulging of the rafts and/or their outward thrusting records significant shortening of the turf in approximate accordance with the deformable slat model. The model can also explain a first-order characteristic of the rupture zone: up-raised mounds (mole tracks) that alternate along strike with fissures or depressions on a wavelength of ~2–3 m, a spacing that was inherited from the original spacing of the R faults. Presumably the apparent deformational "excess" volume of the bulges was matched by a corresponding volume "deficit" in the adjoining depressions or fissures, such that the overall deformation (ignoring any small dilatations) was approximately constant-volume. In detail, the ground deformation was far more complex and irregular than depicted in the cartoon of Figure 9. The occurrence of vertical scarps in the rupture zone and associated development of "calving scars" is one contributing reason for this complexity. Another is that the inter-raft fissures were not rigid "holes," but their walls collapsed under gravity to variably infill the depressions.

The kinematic end members are not mutually exclusive. In the maturing though still coseismic rupture zone, the turf rafts were dissected by secondary faults, fragmenting into isolated blocks as the Y shear zones in which they were embedded accommodated pervasive shearing. At this point, the kinematics of the sheared zones may have more nearly approached that of "ideal transpression." We envision that the blocks continued to rotate within their deforming matrix, with elongate blocks oriented at a high angle to the fault rotating more rapidly than equant-shaped blocks or ones with their long axes aligned subparallel to fault strike (e.g., Ghosh and Ramberg, 1976).

Magnitudes of Slip and Shortening Accommodated by Distributed Deformation of the Rafts

Based on the mean R-fault strikes in the outer rupture zone and their clockwise deflection into the inner rupture zone (Table 1), the deformable slat and ideal transpression models (although based on different assumptions) similarly predict that distributed deformation of the ground materials accommodated a mean finite dextral shear strain of ~1.0–1.5 (Table 2; Fig. 10A). Analyzing turf-raft rotations, the deformable slat model yields a shear strain estimate of 1.2 ± 0.3 as averaged across the seven study sites. The precision of this result implies that this may be a threshold magnitude of rotational strain above which slip became mostly localized into discrete faults. At a given site, the contribution of rotational ground deformation to the overall strike-slip displacement (in meters) can be calculated by multiplying the average finite shear strain (γ) by the mean initial width of its inner rupture zone (W_i; see Fig. 8B). At our study sites, the distributed dextral-slip contribution averages 3.1 ± 1 m using the deformable slat approximation. This amounts to ~34% of the total surface displacement at these sites (Table 2). A corollary is that the remaining ~66% of the strike-slip displacement (on average, ~6.0 m) must have been accommodated by discrete slip on faults—presumably Y-oriented ones. It should be noted that the actual slip proportions (distributed versus discrete) cannot be independently measured by field data because the available (e.g., surveyed) measurements of fault displacement describe the total offset of surface features, such as distorted fence lines or topographic singularities across an aperture width of >3 m (e.g., typical spacing of fence posts), while

TABLE 2. MODELING RESULTS

	Displacement angle (α) (°)	Total displacement magnitude* (m)	Heave (m)	Deformable slat model						Ideal transpression model			
				Distributed shear strain (γ)	Distributed strike slip (m)	Distributed strike slip (% of total)	Raft-parallel shortening magnitude (m)	Fault-perpendicular shortening magnitude (m)	Raft-parallel longitudinal strain (ε) ($\varepsilon = \Delta s / L_o$)	Distributed shear strain (γ)	Distributed strike slip (m)	Distributed strike slip (% of total)	Fault-perpendicular shortening magnitude (m)
			+ve, contractional	dextral	dextral		+ve, contractional	+ve, contractional	+ve, contractional	dextral	dextral		+ve, contractional
Area A, transect 1	−6	10.1	−1.1	0.8	4.3	43	2.0	0.8	0.20	0.6	3.2	31	−0.1
Area A, transect 2	−10	10.1	−1.8	1.5	4.4	45	−0.6	−0.5	−0.24	0.3	1.0	10	−1.5
Area C, transect 1	0	8.9	0.0	1.5	2.9	33	1.5	1.4	0.50	1.5	2.9	33	1.6
Area C, transect 2	8	9.0	1.3	1.7	3.3	37	2.7	2.5	0.63	2.3	4.6	51	3.5
Area C, transect 3	0	9.4	0.0	1.3	2.0	21	1.5	0.9	0.44	1.2	2.0	21	0.9
Area C, transect 4	−12	8.0	−1.7	0.9	2.8	35	0.1	0.0	0.03	0.2	0.6	8	−1.3
Area D, transect 1*	1	3.5	0.1	1.1	1.7	48	0.8	0.8	0.34	1.2	1.7	49	0.8
Mean of sites (n = 7)		**9.3**	**−0.4**	**1.2**	**3.1**	**34**	**1.2**	**0.9**	**0.28**	**1.1**	**2.1**	**25**	**0.6**
1σ		**2.3**	**1.1**	**0.3**	**1.0**	**10**	**1**	**1**	**0.33**	**0.8**	**1.5**	**19**	**1.7**

Notes: See Figure 1C for definition of α, heave, and total displacement; Figure 8B for definition of shear strain (γ); and Figure 2B for transect locations. +ve—positive values. +ve, contractional—positive values defined to be contractional (negative ones, extensional). L_o—original length, Δs—change in length.
*Total displacement value for area D, transect 1 (3.5 m), is excluded from average of site displacements (bold font, bottom row).

Figure 10. (A) Plot of distributed dextral shear strains as calculated from the site-averaged clockwise rotation of Riedel faults between the low-strain, outer part of the rupture zone and the inner high-strain part (Table 2). The *x*-axis strains are based on the deformable slat model, whereas the *y*-axis ones are based on the ideal transpression one. Dashed line has a slope of 45°. (B) Plot of predicted raft-parallel (black dots) or fault-orthogonal (open circles) shortening in the rupture zone of the Kekerengu fault as a function of the fault displacement angle (α). These shortening values were modeled from the observed structural rotation of Riedel faults and the inner rupture zone widths at the various transect sites (Table 1) using the deformable slat model (Table 2; Fig. 8C; Supplemental Material Item S4B [text footnote 1]). Note the crossover from fault-orthogonal extension at α angles <~−10° to fault-orthogonal contraction at greater values. Note that even for a case of slight transtension, (−10° < α < 0°), the turf rafts are expected to experience a net contractile strain, and thus to uplift and form mole tracks. (C) Correlation plot of modeled raft shortening (parallel to their long axis using the deformable slat model; Table 2) versus that measured in the field using area balancing (Table 1). Dashed line has a slope of 45° and represents a perfect correlation (error bars denote two standard deviations on site means). (D) Plot of fracture strike (Riedel faults, R; extension fissures, F) as a function of the coseismic fault displacement angle (α) as averaged at each site (see Fig. 2B for site locations). Open squares and dots depict mean strikes of F and R fractures, respectively, at each site. Error bars are 1σ values for measured strikes at each site (Table 1). The red and black curves are theoretical values for initial fracture strikes as a function of α, based on an assumption of infinitesimal plane strain (to predict stress trajectories) and Mohr-Coulomb failure (to predict fracture attitudes).
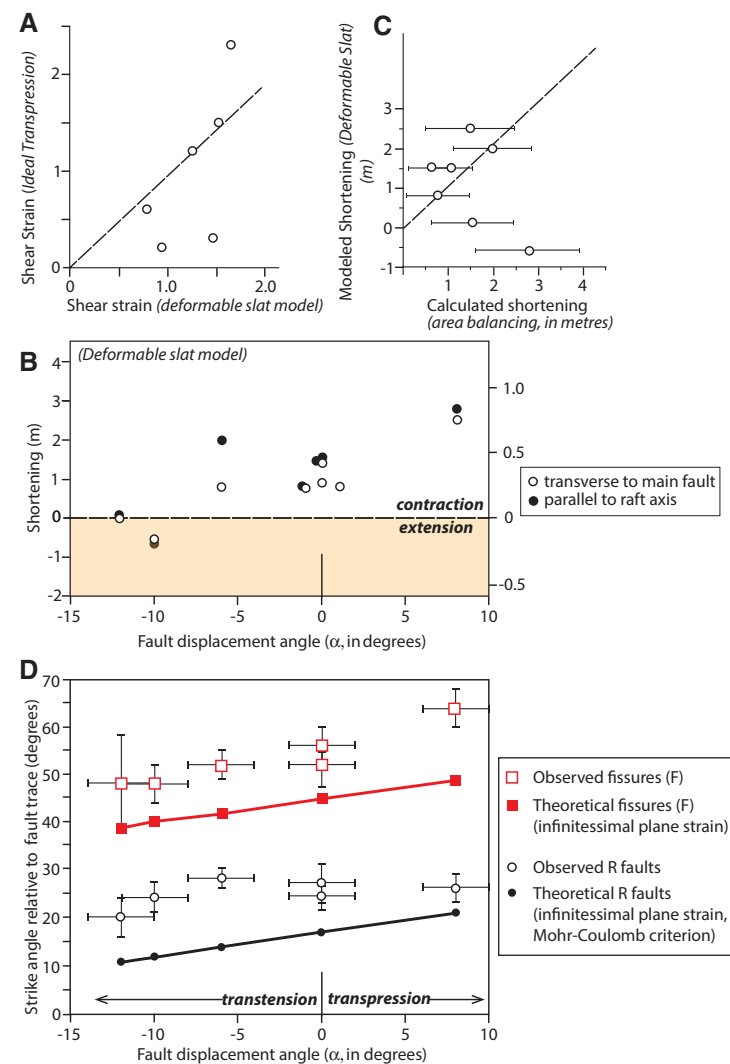
not distinguishing between "distributed" versus "discrete" slip in the way they might have been defined had the scale of resolution been much finer (e.g., Kearse et al., 2018; Howell et al., 2020). While not directly comparable, our identification of an upper threshold for displacement accommodation by rotational deformation of turf rafts in the rupture zone enlarges upon the inference of Litchfield et al. (2014) that a minimum of ~1.5 m of strike slip is required before cracking of the ground is evident.

The deformable slat model predicts a finite internal shortening of rotated turf rafts that is greatest parallel to their length. Oblique to this principal strain direction, a lesser shortening would affect other lines, for example, ones that happen to end up perpendicular to the main fault strike. For our study sites on the Kekerengu fault in 2016, the predicted magnitude of shortening parallel to the mean (rotated) direction of the raft axes averaged ~1.2 m (maximum of ~2.7 m, minimum of −0.6 m), whereas that orthogonal to the main fault averaged ~0.9 (Fig. 10B)—with the difference between these at a given location decreasing as the final strike of the rafts (R_{rot} faults) became more nearly fault perpendicular. Importantly, at any given site, the modeled magnitude of rotation-related shortening was typically ~1–1.5 m greater than the fault heave (strike-perpendicular component of the local displacement vector; Fig. 1C). For example, area C, transect 1, experienced a pure strike-slip displacement ($\alpha = 0°$) with little or no heave, yet the observed rotation of turf rafts at this site implies they must have been shortened internally by ~1.4 m perpendicular the strike of the main fault. Area A, transect 1, hosted a transtensive ($\alpha = -6°$) displacement vector imposing an extensional heave of −1.1 m across the fault. Despite this fault-zone extension, the average rotation of turf rafts at the site predicts their net compressional shortening by +0.8 m in the fault-perpendicular direction (Table 2).

In response to strike-slip without heave (i.e., $\alpha = 0°$), the shear-induced rotation of turf rafts from β_o to β_i requires a compressional shortening of those rafts. With added heave ($\alpha \neq 0°$), the same rotation would be accompanied by either an increase or a decrease in shortening of the raft (relative to the strike-slip case) depending on the sign of that heave. Compressional heave (transpression, $\alpha > 0°$) requires an increase in raft shortening, whereas extensional heave (transtension, $\alpha < 0°$), a decrease. The balance between these competing effects

(rotational shortening versus heave) as applied to the Kekerengu fault in 2016 is illustrated in Figure 10B, which plots displacement angle (α) against total predicted shortening, both parallel to raft axes (black dots) and perpendicular to the main fault (open circles). Note the turnover point between predicted turf raft compression and predicted turf raft extension at a fault displacement angle α of ~−10°. A corollary is that upheaved mole tracks should have been observed along all parts of the rupture zone where the local displacement was at most only slightly transtensive (α >−10°), a prediction that was borne out along the Kekerengu fault in 2016.

Increased shortening magnitude as a result of increased displacement angle (α) implies that if slip was everywhere similar whereas fault strike (and α angle) varied locally along strike, then the average relief (and deformational excess area) of bulges at a particular site should increase as a function of α. In fact, no such correlation between bulge amplitude and the local degree of transpression (angle α) is obvious in the data. Bulge relief varied little across the seven sites (average of 0.47 ± 0.1 m; Table 1). Nor did the mean deformational excess area of the bulges at these sites (1.75 ± 0.8 m^2) vary in a systematic way with displacement angle (α). Assuming a mean detachment depth of ~1.1 ± 0.4 m, the mean deformational excess area implies an overall raft shortening magnitude that averaged 1.6 ± 0.8 m, using simple area balancing (Table 1). By comparison, the deformable slat model predicts that the average shortening value for these sites should have been 1.2 ± 1.0 m (Table 2). In other words, the observations and model predictions, as averaged across the entire data set, are within error of one another. Despite this overall accordance, the model predicts that there should be an increase of shortening (bulge excess area) with increased α (degree of transpression; see Fig 10B), whereas the area balancing-based shortening estimates do not reflect this trend (note lack of linear correlation in Fig. 10C). We infer that the apparent insensitivity of bulge amplitude to local kinematics can be explained by the following two factors, each of which complicates the local relationship between bulge height (or area) and causative shortening: (1) along-strike variations in detachment depth (see Equation 1—deeper depths would generate higher, larger bulges for the same shortening value); and (2) preferential partitioning of the heave component into discrete reverse slip at the scarp rather than as distributed shortening of the turf rafts across the inner rupture zone. Accommodating heave by reverse slip at the scarp means that the distributed heave component is correspondingly reduced. This, in turn, would be expressed by reduced bulge amplitudes (relative to the model) and a smaller observed range in bulge amplitudes, generally. To put it another way, the rotational deformation of the turf rafts preferentially took up the strike-slip component of the displacement, and because this varied little across the study area, bulge amplitudes did not vary much either.

Unusually Large Strike Angle of Synthetic Riedel Faults

A characteristic of the rupture zone of the Kekerengu fault in 2016 was that the acute angle between the main fault trace and the strike of (seemingly unrotated) R faults in its outer rupture zone averaged 25° ± 3° along the length of what was almost a pure strike-slip rupture. If the angle of internal friction, φ, was 30°–39° and the R faults formed in zone of strike-slip simple shearing focused above a mode III strike-slip dislocation, then one would expect synthetic R faults to strike at 15°–19° relative to the Kekerengu fault (Fig. 1A). The prediction assumes an ideal conjugate set of potential Coulomb faults and has been supported by many experiments employing the Riedel boundary condition across a diverse range of analogue materials (e.g., Cloos, 1928; Tchalenko and Ambraseys, 1970; Wilcox et al., 1973; Naylor et al., 1986; Atmaoui et al., 2006). It also agrees with field descriptions of R faults in most natural strike-slip rupture zones (e.g., Tchalenko and Ambraseys, 1970; Rao et al., 2011); however, mean strike angles for R faults of as much as ~20° have been described previously in natural strike-slip earthquake rupture zones, for example, the 2010 Greendale fault earthquake (e.g., Quigley et al., 2012).

What is the significance of the seemingly large, 21°–27° mean R-fault inception angle observed along the Kekerengu fault rupture in 2016? One explanation might be that the slightly transpressional kinematics of the Kekerengu fault caused the direction of maximum instantaneous shortening and compressive stress (σ_1) in its rupture zone to deflect clockwise from the "ideal" strike-slip angle of 45° (e.g., Sanderson and Marchini, 1984; Richard et al., 1995; Teyssier et al., 1995; Schreurs and Colletta, 1998). Figure 10C tests this idea by plotting the mean strike angle (relative to the main fault trace) of R faults observed at our various sites against the local displacement angle (α). It also plots strike angle data for the gaping fissures (F). If the above hypothesis is correct, then there should be a correlation between the strike angles of R and F fractures and the local obliquity of displacement, with the strike of both types of fractures expected to have deflected clockwise with increasing transpression (α angle). The deflection would have been in response to an expected rotation of the principal stress σ_1 (refer to the theoretical curves; these assume plane strain and elastic isotropy). Our field data do not match the theoretical predictions. Interestingly, the mean strike angle of R faults does not seem to increase as a function of α, whereas that of the fissures possibly does increase in that direction, as expected. Regardless, the observed strikes for both fracture types are consistently ~10° more clockwise than indicated by the theoretical curves. Another possible explanation for large strike angles might be that the coefficient of friction of the turf is unusually high, thus causing Coulomb fractures to form at an unusually low angle to σ_1 and at a higher angle to the main fault trace. To explain the R-fault mean angles of ~24° by this means would require a coefficient of friction of >1.0, which is not feasible; nor would it explain extension fissures striking at mean angles >50° to the fault.

To explain the large strike angles, we favor some combination of the following mechanisms: (1) a small, strain-related rotation of fractures in the outer rupture zone; (2) primary hybrid shear-extension fracturing; and/or (3) dynamic boundary conditions differing from a mode III shear fracture at depth. The first of these explanations suggests that the strike angles that we measured for fractures in the outer rupture zone were not original, but (in areas where α = 0°) had been increased from a strike angle of ~17° to ~24° relative to the main

fault as a result of deformational rotation that postdated fracture inception. For ideal transpression, which typically requires slightly less shear strain to accomplish a given rotation than the deformable slat model, the shear strain required to increase mean R-fault strike angles in the outer rupture zone from its predicted theoretical value (this depends on α; see Fig. 10D) to ~24° would be in the range of 1.1–1.9 (maximum 7.1), with this range mostly reflecting between-site differences in α. We believe, but cannot prove, that finite strains of this magnitude were not generally achieved in the outer rupture zone. At four sites where post-earthquake surveys along the eastern Kekerengu fault measured fence lines deflected across a total width <30 m, the deflections recorded dextral shear strains between 0.7 and 3.3, with the higher values invariably focused on the innermost several meters of the rupture zone. However, the resolution of these survey data was limited to the spacing of fence posts (everywhere >3 m), nor did the surveys distinguish between inner and outer rupture zones and the distal deformation zone (Fig. 1C). The second mechanism suggests that in the near surface, where confining pressures are very small, fractures in cohesive turf may initiate as mixed-mode "Griffith" fractures that displace with components of both shear and extension (Fig. 11). If so, such hybrid fractures would be expected to initiate at a higher angle to the main fault than ideal Coulomb shear fractures, thus explaining the larger (~24°) strike angles. Evidence supporting this idea was the extensional gaping that was observed on most R faults in the field; however, such openings need not have been a primary attribute of the faults and could have been acquired later during their rotation and finite evolution. The third mechanism acknowledges that rupturing of the Kekerengu fault was primarily lateral, toward the northeast. The dynamic stress orientations that existed transiently during R-fault inception may not have accorded with the static stresses generated in experiments that employ the "Riedel" boundary condition. Perhaps future studies that employ dynamic rupture modeling to understand stress distributions during earthquakes will clarify our interpretation of R-fault arrays and their geometrical variation.

Paleoseismic Implications

Vertical-axis rotation of decoupled turf strips accounted, on average, for about a third of the large (~10 m) total slip accumulated at the ground surface during the 2016 earthquake. Without linear markers, such as fence lines, this fraction of the coseismic strike slip might not be obvious on the ground after an earthquake. Long after an earthquake, it would be even less obvious on the walls of a paleoseismic trench. There, one might observe one or more deep fissures cutting downward from the paleo–ground surface into a block or raft that had been thrust outward along one or both of its margins over a less-deformed footwall (Figs. 9D, 9E). Depending on the depth extent of the trench and the mechanical properties of the local near-surface stratigraphy, the level of raft uncoupling may or may not be exposed in the trench. Most of the broken-up infill of these fissures would be derived by collapse of near-surface materials that existed prior to the earthquake and would yield radiocarbon ages older
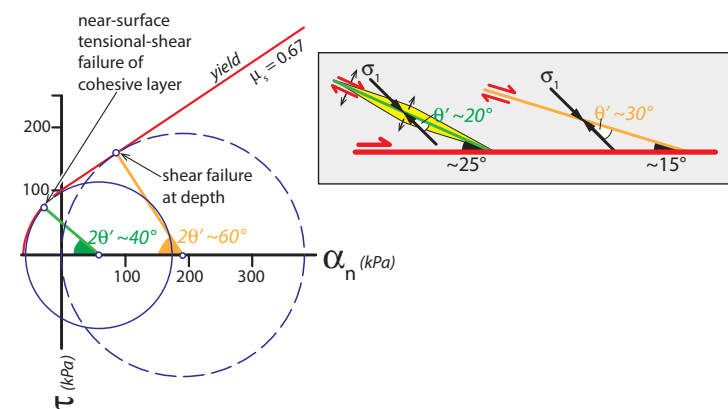
Figure 11. Two-dimensional Mohr circle–based interpretation of the relatively large (~25°) angle between the main Kekerengu fault trace and the strike of synthetic Riedel faults that formed during early stages of the 2016 earthquake rupture. *kPa*—kiloPascals of stress. μ_s—coefficient of static friction (dimensionless).

than—or perhaps approximately the same age as—the paleoearthquake. Where observed, geometric relationships between the steep-sided fissures, low-angle thrust faults (actually oblique-slip faults), and steeply dipping strike-slip faults (or shear zones) might be cross-cutting—as if this plexus of faults resulted from multiple events—yet the all these structures may have formed (though not necessarily at the same instant in time) during a single large-slip earthquake. In addition, the contractional kinematics of the low-angle oblique-reverse faults may lead a geologist to infer that the master fault at depth had slipped with a contractional sense of heave (that is, with a reverse sense of dip slip), when in fact the displacement may have been strike slip or even slightly transtensional. The contraction occurs because of rotation of elongate rafts and lateral transfer of material into the plane of the trench as a result of strike slip.

■ CONCLUSIONS

In coherent or clay-rich surficial materials, earthquake ruptures experiencing large strike-slip displacements (~10 m) cause a large finite deformation in detached turf rafts bounded by deformed Riedel faults or extensional fissures. Pressure bulges initiate in the stepovers between adjacent R faults. As slip accrues, these "mole tracks" amplify and widen as the turf rafts are rotated about a vertical axis and internally shortened. As this happens, the initially synthetic offset on an R fault is inverted into an antithetic one, and gaping fissures, partially infilled with collapsed debris, open up along the trace of the R fault.

Along the Kekerengu fault after the 2016 Kaikōura earthquake, the decoupled layer of deformed near-surface materials consisted of clay-silt–rich sediment

densely matted by grass at the top and was mostly ~1 m thick. Deformed turf rafts are bounded on one or both sides by low-angle contractional faults that emplace the shortened mass of turf outward over less-deformed ground. Eventually individual turf rafts became fragmented into blocks by numerous short secondary ("2") fractures striking at a high angle to the main fault. We interpret these as antithetic Riedel faults. As further slip accrued, blocks were dispersed into strongly sheared earth of the inner rupture zone and further rotated, with elongate blocks at a high angle to the fault rotating more rapidly than equant-shaped blocks.

The deformable slat model approximates the kinematics of distributed ground deformation during the early stages of coseismic slip when the turf rafts are rotating. Along the Kekerengu fault, this rotation averaged ~20°–30°, accommodating a finite shear strain of 1.0–1.5 and an equivalent strike slip of ~3–4 m. The remaining ~6 m of coseismic strike slip accrued as translational slip on discrete Y faults. Rotational deformation of the turf rafts preferentially took up the strike-slip component of displacement, whereas the small component of heave was chiefly accommodated by discrete dip slip.

Whereas the average contractional heave on the Kekerengu fault averaged <10 cm, internal shortening of the turf rafts averaged ~1.5 m parallel to the (clockwise-rotated) long axes of the rafts, and ~1 m as measured exactly perpendicular to the strike of the main fault. This contractional bulging is chiefly driven by rotation and may mislead one into inferring that the local kinematics of fault slip was transpressional. In fact, pressure bulging and "mole tracks" are probably characteristic features of not only most pure strike-slip and transpressional ruptures, but also those that are slightly transtensional ($-10° < \alpha < 0°$).

Contrary to the predictions of simple Coulomb theory, Riedel faults may strike at a relatively large (i.e., 20°–30°) angle to the main fault trace. We attribute this to some combination of strain-related rotation of fractures, hybrid shear-extension fracturing, and dynamic boundary conditions associated with the propagating rupture.

In a paleoseismic trench perpendicular to a strike-slip fault that has experienced large coseismic displacements, one might observe deep fissures, low-angle (oblique) thrust faults, and steeply dipping strike-slip faults, some cross-cutting one another, yet all may have formed at different instants during the same earthquake. The contractional kinematics of the low-angle thrust faults does not require that the master fault at depth also has a reverse component of slip—indeed it might be slightly extensional.

REFERENCES CITED

Ando, R., and Kaneko, Y., 2018, Dynamic rupture simulation reproduces spontaneous multifault rupture and arrest during the 2016 Mw 7.9 Kaikōura earthquake: Geophysical Research Letters v. 45, p. 12,875–12,883, https://doi.org/10.1029/2018GL080550.

Armijo, R., Tapponier, P., and Tonglin, H., 1989, Late Cenozoic right-lateral strike-slip faulting in southern Tibet: Journal of Geophysical Research, v. 94, p. 2787–2838, https://doi.org/10.1029/JB094iB03p02787.

Atmaoui, N., Kukowski, N., Stöckhert, B., and König, D., 2006, Initiation and development of pull-apart basins with Riedel shear mechanism: Insights from scaled clay experiments: International Journal of Earth Sciences, v. 95, p. 225–238, https://doi.org/10.1007/s00531-005-0030-1.

Beavan, J., Tregoning, P., Bevis, M., Kato, T., and Meertens, C., 2002, Motion and rigidity of the Pacific Plate and implications for plate boundary deformation: Journal of Geophysical Research, v. 107, 2261, https://doi.org/10.1029/2001JB000282.

Bergerat, F., Angelier, J., Gudmundsson, A., and Torfason, H., 2003, Push-ups, fracture patterns, and palaeoseismology of the Leirubakki Fault, South Iceland: Journal of Structural Geology, v. 25, p. 591–609, https://doi.org/10.1016/S0191-8141(02)00051-2.

Bowman, D., King, G.C.P., and Tapponier, P., 2003, Slip partitioning by elastoplastic propagation on oblique slip at depth: Science, v. 300, p. 1121–1123, https://doi.org/10.1126/science.1082180.

Cambonie, T., Klinger, Y., and Lazarus, V., 2018, Similarities between mode III crack growth patterns and strike-slip faults: Philosophical Transactions of the Royal Society of London A., v. 377, 20170392, https://doi.org/10.1098/rsta.2017.0392.

Carrivick, J.L., Smith, M.W., and Quincey, D.J., 2016, Structure from Motion in the Geosciences: Chichester, UK, John Wiley and Sons, 197 p., https://doi.org/10.1002/9781118895818.

Cesca, S., Zhang, Y., Mouslopoulou, V., Wang, R., Saul, J., Savage, M., Heimann, S., Kufner, S.-K., Oncken, O., and Dahm, T., 2017, Complex rupture process of the Mw 7.8, 2016, Kaikoura earthquake, New Zealand, and its aftershock sequence: Earth and Planetary Science Letters, v. 478, p. 110–120, https://doi.org/10.1016/j.epsl.2017.08.024.

Cloos, H., 1928, Experimente zur innneren Tektonik: Centralblatt fur Mineralogie, v. 12, p. 609–621.

Deng, Q., Wu, D., Zhang, P., and Chen, S., 1986, Structure and deformational character of strike-slip fault zones: Pure and Applied Geophysics, v. 124, p. 203–223, https://doi.org/10.1007/BF00875726.

Dooley, T.P., and Schreurs, G., 2012, Analogue modelling of intraplate strike-slip tectonics: A review and new experimental results: Tectonophysics, v. 574–575, p. 1–71, https://doi.org/10.1016/j.tecto.2012.05.030.

Ghosh, S.K., and Ramberg, H., 1976, Reorientation of inclusions by a combination of pure shear and simple shear: Tectonophysics, v. 34, p. 1–70, https://doi.org/10.1016/0040-1951(76)90176-1.

Hamling, I.J., Hreinsdóttir, S., Clark, K., Elliott, J., Liang, C., Fielding, E., Litchfield, N., Villamor, P., Wallace, L., Wright, T.J., D'Anastasio, E., Bannister, S., Burbidge, D., Denys, P., Gentle, P., Howarth, J., Mueller, C., Palmer, N., Pearson, C., Power, W., Barnes, P., Barrell, D.J.A., Van Dissen, R., Langridge, R., Little, T., Nicol, A., Pettinga, J., Rowland, J., and Stirling, M., 2017, Complex multifault rupture during the 2016 Mw 7.8 Kaikōura earthquake, New Zealand: Science, v. 356, eaam7194, https://doi.org/10.1126/science.aam7194.

Hill, M.P., 2020, Compilation and modelling of remotely piloted aircraft system images captured after the 2016 Mw 7.8 Kaikoura earthquake: GNS Science Report 2020/14.

Holden, C., Kaneko, Y., D'Anastasio, E., Benites, R., Fry, B., and Hamling, I.J., 2017, The 2016 Kaikōura earthquake revealed by kinematic source inversion and seismic wavefield simulations: Slow rupture propagation on a geometrically complex crustal fault network: Geophysical Research Letters, v. 44 p. 11,320–11,328, https://doi.org/10.1002/2017GL075301.

Howell, A., Nissen, E., Stahl, T., Clark, K., Kearse, J., Van Dissen, R., Villamor, P., Langridge, R., and Jones, K., 2020, Three-dimensional surface displacements during the 2016 Mw 7.8 Kaikōura earthquake (New Zealand) from photogrammetry-derived point clouds: Journal of Geophysical Research: Solid Earth, v. 125, e2019JB018739, https://doi.org/10.1029/2019JB018739.

Jin, H., and Wang, H., 2009, Estimation of the 2001 Kunlun earthquake fault slip from GPS coseismic data using Hori's inverse method: Earthquake Science, v. 22, p. 609–614, https://doi.org/10.1007/s11589-009-0609-x.

Kaiser, A., Balfour, N., Fry, B., Holden, C., Litchfield, N., Gerstenberger, M., D'Anastasio, E., Horspool, N., McVerry, G., Ristau, J., Bannister, S., Christophersen, A., Clark, K., Power, W., Rhoades, D., Massey, C., Hamling, I., Wallace, L., Mountjoy, J., Kaneko, Y., Benites, R., Van Houtte, C., Dellow, S., Wotherspoon, L., Elwood, K., and Gledhill, K., 2017, The 2016 Kaikōura, New Zealand, earthquake: Preliminary seismological report: Seismological Research Letters, v. 88, p. 727–739, https://doi.org/10.1785/0220170018.

Kearse, J., Little, T.A., Van Dissen, R.J., Barnes, P.M., Langridge, R., Mountjoy, J., Ries, W., Villamor, P., Clark, K.J., Benson, A., Lamarche, G., Hill, M., and Hemphill-Haley, M., 2018, Onshore to offshore ground surface and seabed rupture of the Jordan-Kekerengu-Needles fault network during the 2016, Mw 7.8 Kaikōura earthquake, New Zealand: Bulletin of the Seismological Society of America, v. 108, p. 1573–1595, https://doi.org/10.1785/0120170304.

Kearse, J., Kaneko, Y., Little, T., and Van Dissen, R., 2019, Curved slickenlines preserve direction of rupture propagation: Geology, v. 47, p. 838–842, https://doi.org/10.1130/G46563.1.

Koto, B., 1893, On the cause of the great earthquake in central Japan, 1891: Journal of College Sciences (Imperial University, Japan), v. 5, no. 4, p. 296–353.

Lin, A., and Nishikawa, M., 2011, Riedel shear structures in the co-seismic surface rupture zone produced by the 2001 M_w 7.8 Kunlun earthquake, northern Tibetan Plateau: Journal of Structural Geology, v. 33, p. 1302–1311, https://doi.org/10.1016/j.jsg.2011.07.003.

Lin, A., Guo, J., and Fu, B., 2004, Co-seismic mole track structures produced by the 2001 M_s 8.1 Central Kunlun earthquake, China: Journal of Structural Geology, v. 26, p. 1511–1519, https://doi.org/10.1016/j.jsg.2004.01.005.

Lin, A., Rao, G., Jia, D., Wu, X., Yan, B., and Ren, Z., 2011, Co-seismic strike-slip surface rupture and displacement produced by the 2010 M_w 6.9 Yushu earthquake, China, and implications for Tibetan tectonics: Journal of Geodynamics, v. 52, p. 249–259, https://doi.org/10.1016/j.jog.2011.01.001.

Litchfield, N.J., Van Dissen, R.J., Hornblow, S., Quigley, M., and Archibald, G., 2014, Detailed analysis of Greendale Fault ground surface rupture displacements and geometries: GNS Science Report 2013/18, 166 p.

Litchfield, N.J., et al., 2018, Surface rupture of multiple crustal faults in the M_w 7.8 2016 Kaikōura, New Zealand, earthquake: Bulletin of the Seismological Society of America, v. 108, p. 1496–1520, https://doi.org/10.1785/0120170300.

Little, T.A., Van Dissen, R., Kearse, J., Norton, K., Benson, A., and Wang, N., 2018, Kekerengu fault, New Zealand: Timing and size of Late Holocene surface ruptures: Bulletin of the Seismological Society of America, v. 108, p. 1556–1572, https://doi.org/10.1785/0120170152.

Mandl, G., 1987, Tectonic deformation by rotating parallel faults: The "bookshelf" mechanism: Tectonophysics, v. 141, p. 277–316, https://doi.org/10.1016/0040-1951(87)90205-8.

Morris, P., 2020, Accommodating ~9 m of dextral slip on the Kekerengu Fault through ground deformation during the Mw 7.8 Kaikōura Earthquake, November 2016 [M.S. thesis]: Wellington, New Zealand, Victoria University of Wellington, 162 p.

Naylor, M.A., Mandl, G., and Sijpeseijn, C.H.K., 1986, Fault geometries in basement-induced wrench faulting under different initial stress states: Journal of Structural Geology, v. 8, p. 737–752, https://doi.org/10.1016/0191-8141(86)90022-2.

Nur, A., Ron, H., and Scotti, O., 1986, Fault mechanics and the kinematics of block rotations: Geology, v. 14, p. 746–749, https://doi.org/10.1130/0091-7613(1986)14<746:FMATKO>2.0.CO;2.

Oettle, N.K., and Bray, J.D., 2013, Fault rupture propagation through previously ruptured soil: Journal of Geotechnical and Geoenvironmental Engineering, v. 139, p. 1637–1647, https://doi.org/10.1061/(ASCE)GT.1943-5606.0000919.

Quigley, M., Van Dissen, R., Litchfield, N., Villamor, P.B.D., Barrel, D., Furlong, K., Stahl, T., Bilderback, E., and Noble, D., 2012, Surface rupture during the 2010 M_w 7.1 Darfield (Canterbury) earthquake: Implications for fault rupture dynamics and seismic-hazard analysis: Geology, v. 40, p. 55–58, https://doi.org/10.1130/G32528.1.

Rao, G., Lin, A., Yan, B., Dong, J., Wu, X., and Ren, Z., 2011, Co-seismic Riedel shear structures produced by the 2010 M_w 6.9 Yushu earthquake, central Tibetan Plateau, China: Tectonophysics, v. 507, p. 86–94, https://doi.org/10.1016/j.tecto.2011.05.011.

Richard, P.D., Naylor, M.A., and Koopman, A., 1995, Experimental models of strike-slip tectonics: Petroleum Geoscience, v. 1, p. 71–80, https://doi.org/10.1144/petgeo.1.1.71.

Riedel, W., 1929, Zur Mechanik geologischer Brucherscheinungun: Centralblatt Mineralogie, Abteilung B, p. 354–368.

Sanderson, D.J., and Marchini, W.R.D., 1984, Transpression: Journal of Structural Geology, v. 6, p. 449–458, https://doi.org/10.1016/0191-8141(84)90058-0.

Schreurs, G., 1994, Experiments on strike-slip faulting and block rotation: Geology, v. 22, p. 567–570, https://doi.org/10.1130/0091-7613(1994)022<0567:EOSSFA>2.3.CO;2.

Schreurs, G, 2003, Fault development and interaction in distributed strike-slip shear zones: An experimental approach, in Storti, F., Holdsworth, R.E., and Salvini, F., eds., Intraplate Strike-Slip Deformation Belts: Geological Society of London Special Publication 210, p. 35–52, https://doi.org/10.1144/GSL.SP.2003.210.01.03.

Schreurs, G., and Colletta, B., 1998, Analogue modelling of faulting in zones of continental transpression and transtension, in Strachen, R.E., Holdsworth, R.A., and Dewey, J.F., eds., Continental Transpressional and Transtensional Tectonics: Geological Society of London Special Publication 135, p. 59–79, https://doi.org/10.1144/GSL.SP.1998.135.01.05.

Tchalenko, J.S., and Ambraseys, N.N., 1970, Structural analysis of the Dasht-e Bayaz (Iran) earthquake fractures: Geological Society of America Bulletin, v. 81, p. 41–60, https://doi.org/10.1130/0016-7606(1970)81[41:SAOTDB]2.0.CO;2.

Terres, R.R., and Sylvester, A.G., 1981, Kinematic analysis of rotated fractures and blocks in simple shear: Bulletin of the Seismological Society of America, v. 71, p. 1593–1605.

Teyssier, C., Tikoff, B., and Markley, M., 1995, Oblique plate motion and continental tectonics: Geology, v. 23, p. 447–450, https://doi.org/10.1130/0091-7613(1995)023<0447:OPMACT>2.3.CO;2.

Wilcox, R.E., Harding, T.P., and Seely, D.R., 1973, Basic wrench tectonics: American Association of Petroleum Geologists Bulletin, v. 57, p. 74–96, https://doi.org/10.1306/819A424A-16C5-11D7-8645000102C1865D.

Zekkos, D., Manousakis, J., Athanasopoulos-Zekkos, A., Clark, M., Knoper, L., Massey, C., Archibald, G., Greenwood, W., Hemphill-Haley, M., Rathje, E., Litchfield, N., Medwedeff, W., Van Dissen, R.J., Kearse, J., Ries, W., Villamor, P., and Langridge, R.M., 2018, Structure-from-Motion based 3D mapping of landslides & fault rupture sites during 2016 Kaikōura earthquake reconnaissance: Proceedings, Eleventh U.S. National Conference on Earthquake Engineering Integrating Science, Engineering & Policy, Los Angeles, California, 25–29 June, 11 p.

Zinke, R., Hollingsworth, J., Dolan, J.F., and Van Dissen, R., 2019, Three-dimensional surface deformation in the 2016 M_W 7.8 Kaikōura, New Zealand, earthquake from optical image correlation: Implications for strain localization and long-term evolution of the Pacific-Australian plate boundary: Geochemistry Geophysics Geosystems, v. 20, p. 1609–1628, https://doi.org/10.1029/2018GC007951.